

# SATURN'S GREAT STORM OF 2010-2011: EVIDENCE FOR AMMONIA AND WATER ICES FROM ANALYSIS OF VIMS SPECTRA.

L.A. SROMOVSKY, K. H. BAINES, AND P. M. FRY

Space Science and Engineering Center, University of Wisconsin-Madison  
 1225 West Dayton Street, Madison, WI 53706

*Journal reference: Icarus 226 (2013) 402-418.*

## ABSTRACT

Our analysis of Cassini/VIMS near-infrared spectra of Saturn's Great Storm of 2010-2011 reveals a multi-component aerosol composition comprised primarily of ammonia ice, with a significant component of water ice. The most likely third component is ammonium hydrosulfide or some weakly absorbing material similar to what dominates visible clouds outside the storm region. Horizontally heterogeneous models favor ammonium hydrosulfide as the third component, while horizontally uniform models favor the weak absorber. Both models rely on water ice absorption to compensate for residual spectral gradients produced by ammonia ice from  $3.0\ \mu\text{m}$  to  $3.1\ \mu\text{m}$  and need the third component to fill in the sharp ammonia ice absorption peak near  $2.96\ \mu\text{m}$ . The best heterogeneous model has spatial coverage fractions of 55% ammonia ice, 22% water ice, and 23% ammonium hydrosulfide. The best homogeneous model has an optically thin layer of weakly absorbing particles above an optically thick layer of water ice particles coated by ammonia ice. This is the first spectroscopic evidence of water ice in Saturn's atmosphere, found near the level of Saturn's visible cloud deck where it could only be delivered by powerful convection originating from  $\sim 200\ \text{km}$  deeper in the atmosphere.

*Subject headings:* Saturn; Saturn, Atmosphere; Atmospheres, composition; Atmospheres, dynamics

## 1. INTRODUCTION

Beginning in early December of 2010 amateur astronomers around the world observed the outbreak of a remarkably large storm in the atmosphere of Saturn (Sánchez-Lavega et al. 2011). This large feature is the sixth known of a class of features historically referred to as Great White Spots, which have occurred at roughly thirty year intervals (Sánchez-Lavega et al. 1991), i.e. at intervals close to one Saturnian year, always in the northern hemisphere, and usually in that hemisphere's summer. This is the first such storm observed close up by a spacecraft (Cassini) in orbit around Saturn. The Cassini Imaging Science Subsystem (ISS) captured images of the storm beginning in December (Fig. 1) and the Visual and Infrared Mapping Spectrometer (VIMS) captured its first spectra of the storm in February 2011 (Fig. 2). It was then centered at  $35^\circ\ \text{N}$  and covered about  $7^\circ$  in latitude, with a long and widening downstream plume. The vertical and horizontal scale of its effects were probed by thermal infrared spectroscopy, which showed that within a month the storm generated large perturbations of atmospheric temperatures, winds, and composition over a wide area between  $20^\circ\ \text{N}$  and  $50^\circ\ \text{N}$  (Fletcher et al. 2011b). Dynamical models of such storms (Hueso and Sánchez-Lavega 2004) suggest that they originate at the 10-12 bar level where water vapor condensation is expected, and generate enormous convective towers reaching pressures as low as  $\sim 150\ \text{mb}$ . It is thus conceivable that these storms provide a window into the deeper layers of Saturn's atmosphere.

The near-IR spectral observations of VIMS (from  $1\ \mu\text{m}$  to  $5.15\ \mu\text{m}$ ) are of special interest because they are particularly diagnostic of cloud particle composition. It was immediately obvious from VIMS spectra that the cloud particles in this storm had an unusual composition;

they displayed a surprisingly strong absorption near  $3\ \mu\text{m}$  (Baines et al. 2011) that was not seen anywhere else on Saturn (Fig. 2). Ammonia ice ( $\text{NH}_3$ ) and ammonium hydrosulfide ( $\text{NH}_4\text{SH}$ ), as well as water ice, are possible contributors because they are all strong absorbers in this region of the spectrum. While all of these molecules are also expected to produce clouds on Saturn, a thick overlying haze has largely shielded them from view. Until recently, there has been little spectroscopic evidence of any of them except in association with small storm clouds in the southern hemisphere, where excess absorption near  $2.7\ \mu\text{m}$  suggested the presence of freshly condensed  $\text{NH}_3$  (Baines et al. 2009). The Great Storm of 2010-2011 is by far the largest  $3\text{-}\mu\text{m}$  absorbing feature ever seen on Saturn and provides the best opportunity for detailed spectroscopic analysis.

Our objective here is to model the composition and vertical structure of the storm feature, using detailed spectral characteristics to determine the dominant components of the storm cloud particles, as well as to estimate the size of the particles and whether they are likely to be composite or pure. Of all the pure substances we tried, particles of  $\text{NH}_3$  provided the best fit to the absorption feature. However, pure  $\text{NH}_3$  presents problems because its narrow strong absorption feature at  $2.96\ \mu\text{m}$ , which should be resolved by VIMS, is seen only weakly if at all. Other characteristics of  $\text{NH}_3$  do appear to fit well, but some mechanism that suppresses the  $2.96\text{-}\mu\text{m}$  feature seems to be required. Contributions of other absorbers such as  $\text{NH}_4\text{SH}$  and water ice can provide improved fits, suggesting that all three substances might be present in the cloud particles, with  $\text{NH}_3$  being the most prominent contributor and water the most probable secondary component. In the following we first present the VIMS observations, describe our spectral analysis techniques, evaluate spectral fits for pure substances, then

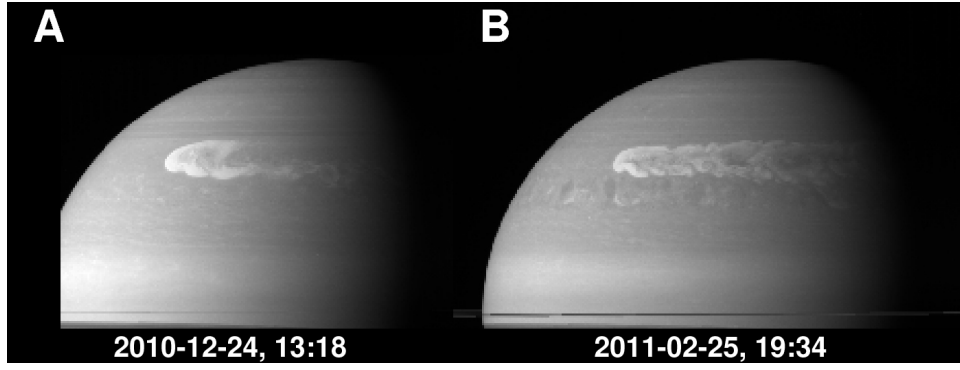


FIG. 1.— Cassini ISS images of Saturn’s Great Storm of 2010-2011 (A) at an early stage of development in December 2010 and (B) at approximately the same time as the first VIMS spectral images obtained in February 2011. Both images were made with a CB2 filter (752 nm) and the wide angle camera.

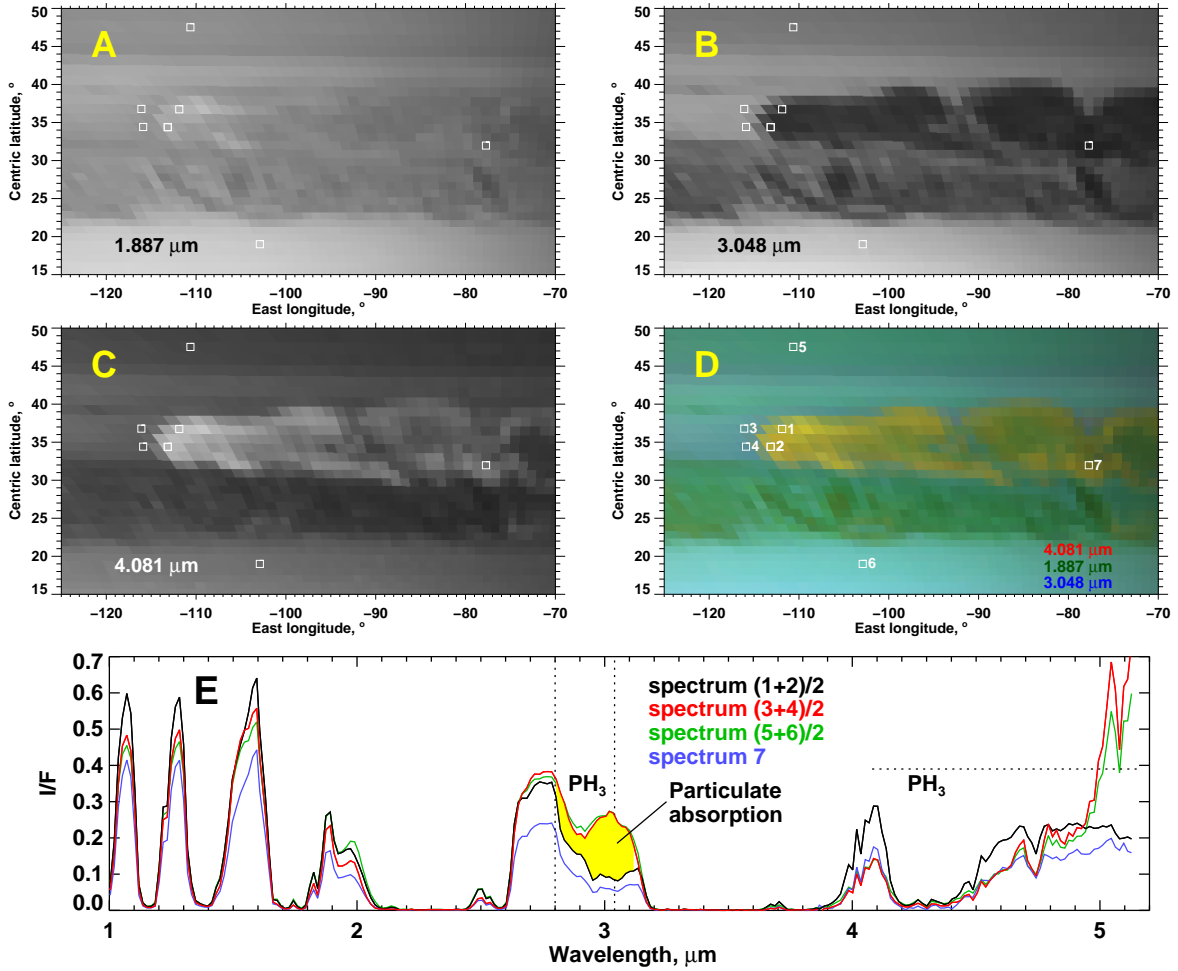


FIG. 2.— (A–C) VIMS spectral images of the storm in February 2011, sampled at wavelengths indicated within each panel, remapped to an orthogonal projection, and linearly stretched so that white corresponds to a reflectivity ( $I/F$ ) of 0.4. The color composite (D) is created from spectral images at 3.048  $\mu\text{m}$  (blue component), 1.887  $\mu\text{m}$  (green component), and 4.081  $\mu\text{m}$  (red component). Numbered boxes indicate the locations at which spectral samples (E) were obtained. Here closely similar spectra are averaged to simplify the figure. Strong absorption at 3.048  $\mu\text{m}$  reduces the blue contribution in the color composite image, making the storm feature appear orange. The parts of the storm that are bright at 4.081  $\mu\text{m}$  (locations 1 and 2, for example) are much darker at 3.048  $\mu\text{m}$  than the region ahead of the storm (locations 3 and 4). 1.887  $\mu\text{m}$  and 4.081  $\mu\text{m}$  are pseudo-continuum wavelengths, subject to little gas absorption, and thus show reflective properties of clouds more directly. The strong reflectivity at 4.081  $\mu\text{m}$  indicates that the cloud particles are relatively large ( $\sim 1 \mu\text{m}$  or more). The spectra from regions 3–6 are very similar, especially in the 2.9–3.04  $\mu\text{m}$  region where they contain a similar phosphine absorption feature. The difference between those spectra and the storm head spectra (1 and 2) is colored yellow to show the extra absorption that is mainly due to particulates.

consider alternatives involving combinations of  $\text{NH}_3$  with other substances, both as co-mingled pure particles and

as composite particles, and also as layers of different compositions.

## 2. OBSERVATIONS.

We used publicly available spectra acquired by VIMS during 24 February 2011 at 00:36:36 UT, data cube number 1677201862.3, acquired under observation name VIMS\_145SA\_WIND5HR001, at a phase angle of  $52^\circ$  and a range of  $1.84 \times 10^6$  km. The VIMS instrument and investigation are described by Miller et al. (1996) and Brown et al. (2004). The instrument's spectral range is  $0.35\text{--}5.1\ \mu\text{m}$ , with an effective pixel size of 0.5 milliradian on a side and a near-IR spectral resolution of approximately 15 nm (sampled at intervals of approximately 16 nm). The atmospheric pressures that can be sampled by this wide spectral range are indicated in Fig. 3, which was computed for a clear atmosphere and thus over-estimates the penetration depths below the 300 mb level, where significant aerosol opacity is a limiting factor. Methane is the most prominent absorbing gas at most wavelengths. Hydrogen collision-induced absorption is dominant in the  $1.95\text{--}2.15\ \mu\text{m}$  range. Phosphine is prominent in the  $2.8\text{--}3\ \mu\text{m}$  and  $4.2\text{--}5\ \mu\text{m}$  regions. Arsine and  $\text{CH}_3\text{D}$  have much smaller effects, and germane has too small an effect to be noticed in our investigation.

A selection of these earliest VIMS observations of the Great Storm are shown in Fig. 2. Remapped images are shown at three key wavelengths and spectra from seven representative locations are displayed, including means of two just upstream of the storm head and two within the storm head itself. Compared to spectra at other locations, the cloud reflectivities in the storm head are the highest at  $4.081\ \mu\text{m}$  and the lowest at  $3.048\ \mu\text{m}$ . As shown in Fig. 2E, spectra obtained upstream (locations 3 & 4) display absorption between 2.8 and  $3\ \mu\text{m}$  that is due to phosphine, but show little absorption at  $3.05\ \mu\text{m}$ . The upstream clouds are also more transparent at thermal wavelengths, evident from their large apparent I/F values near  $5\ \mu\text{m}$ . The storm particles are brighter than the upstream cloud particles in most window regions, somewhat more absorbing at  $2.7\ \mu\text{m}$ , but dramatically more absorbing at  $3.048\ \mu\text{m}$ . The image at  $1.887\ \mu\text{m}$  (Fig. 2A) is used for the green component of the composite image because it provides the closest match to the I/F at  $3.05\ \mu\text{m}$  for those regions that do not contain a  $3\text{-}\mu\text{m}$  particle absorption, both of which, along with  $4.081\ \mu\text{m}$ , are pseudo continuum wavelengths that are relatively unaffected by gas absorption. This means that the ratio of I/F at  $3.048\ \mu\text{m}$  to that at  $1.887\ \mu\text{m}$  should be a good measure of the degree of  $3\text{-}\mu\text{m}$  absorption, as illustrated in Fig. 4. The regions of high reflectivity at  $4.081\ \mu\text{m}$  are places where the cloud particles are relatively large (probably  $1\ \mu\text{m}$  or more), and strong absorption at  $3.048\ \mu\text{m}$  (Fig. 2B) appears as bright orange in the color composite (Fig. 2D).

## 3. VIMS INSTRUMENT CHARACTERISTICS AND CORRECTIONS

Before proceeding with the quantitative analysis of the VIMS spectra, we first describe special characteristics of the VIMS instrument and summarize how we handle data processing, photometry, and navigation.

### 3.1. VIMS responsivity errors and corrections

The responsivity of the VIMS detector array is significantly reduced at joints between order sorting filters, which occur at wavelengths of  $1.64\ \mu\text{m}$ ,  $2.98\ \mu\text{m}$ , and

$3.85\ \mu\text{m}$  (Miller et al. 1996; Brown et al. 2004). The decline is most severe at  $1.64\ \mu\text{m}$  and  $3.85\ \mu\text{m}$ , and VIMS spectra in these regions cannot be trusted, as shown by Sromovsky and Fry (2010b) for the  $1.64\ \mu\text{m}$  joint, and by our own radiation transfer modeling for the  $3.85\ \mu\text{m}$  joint. The spectra near the  $2.98\text{-}\mu\text{m}$  joint are reasonably well corrected in spectra obtained during the Jupiter encounter, as shown by Sromovsky and Fry (2010b), but minor problems are present in the VIMS spectra of Saturn. The  $2.98\text{-}\mu\text{m}$  joint is unfortunately located so close to the prominent  $\text{NH}_3$  ice feature near  $2.96\text{-}\mu\text{m}$  that its effects can be misinterpreted as being due to the presence of  $\text{NH}_3$  ice. In fact, all the raw VIMS spectra of Saturn do contain a dip very similar to what might be produced by a small component of  $\text{NH}_3$  ice in the main tropospheric haze layer. However, the spatial variation of the feature is much more easily understood as an instrumental artifact. The feature appears to be a fractional effect with no dependence on latitude or view angle, but only on the x-coordinate of the VIMS spectral data cube. It is not plausible that an atmospheric effect could produce this characteristic. Our interpretation is confirmed by ISO measurements of Saturn's  $3\text{-}\mu\text{m}$  spectrum by Encrenaz et al. (1999), which provide no evidence of such a feature.

To correct for the responsivity error caused by the  $2.98\text{-}\mu\text{m}$  filter joint we collected spectra covering regions without strong convective features, then interpolated across the artifact for each spectrum and used the fractional depression below the interpolated line as a measure of the responsivity error that needed to be corrected. We found essentially no variation along image columns (y-direction), and thus used an average fractional depression along each column to define the correction for any position along a column. We did find a significant variation perpendicular to the column direction, however. The fractional error for band 127 varied smoothly from 0.75 at column zero to 0.52 at column 63, a change that is about 30 times the standard deviation along that column. A physical explanation for this behavior in terms of instrument design and operation remains to be determined. With this correction we are able to separate the effects of the filter joint from those of true particulate absorption in the same region of the spectrum.

### 3.2. VIMS errors at low signal level

Although a specific cause has not been identified, Sromovsky and Fry (2010b) showed that very dark regions of VIMS spectra tend to be significantly brighter than independent observations from the ground and from HST using NICMOS. This occurs at very low signal levels, for which the instrument is responding with 1 Digital Number or less. What appears to be a small offset, just a fraction of a DN, if not corrected for, leads to excessive stratospheric haze opacity in models designed to match these spectra. As we have no well-defined correction for this effect, it limits our ability to constrain the stratospheric haze, which is only noticed at wavelengths for which the atmosphere is extremely dark because of strong gas absorption.

### 3.3. VIMS wavelength corrections

The wavelength calibration that worked well for modeling VIMS Jupiter spectra (Sromovsky and Fry 2010b)

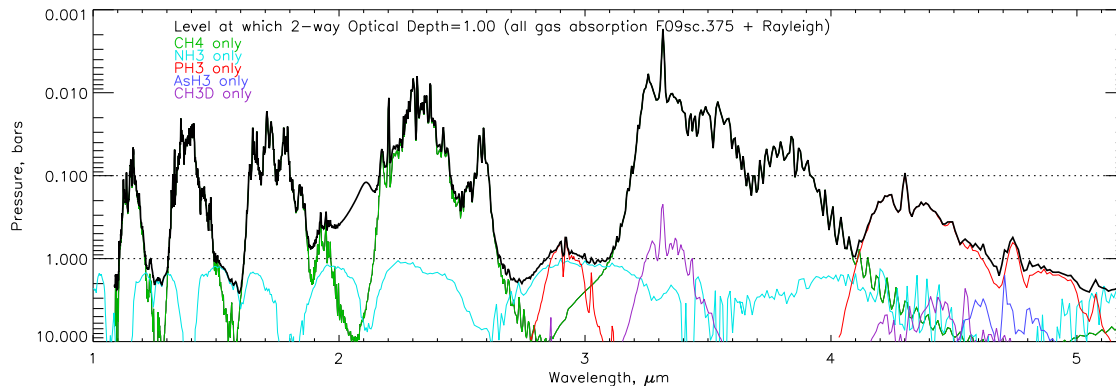


FIG. 3.— Penetration depth of near-IR photons indicated by pressures at which a unit albedo reflecting layer produces an external I/F of  $1/e$  at normal incidence and viewing. Left: the CCD spectral region. Curves are shown for methane only (green), ammonia only (cyan), phosphine only (red), arsine only (blue),  $\text{CH}_3\text{D}$  only (purple), and all gases combined (black), assuming the Lindal et al. (1985) temperature profile, the  $\text{He}/\text{H}_2$  ratio of Conrath and Gautier (2000), the ammonia profile of Prinn et al. (1984), and the phosphine profile of Fletcher et al. (2009a) with a scale height of 0.375 times the gas scale height. Included, but not shown separately, is  $\text{H}_2$  CIA, which peaks near  $2.1 \mu\text{m}$ .

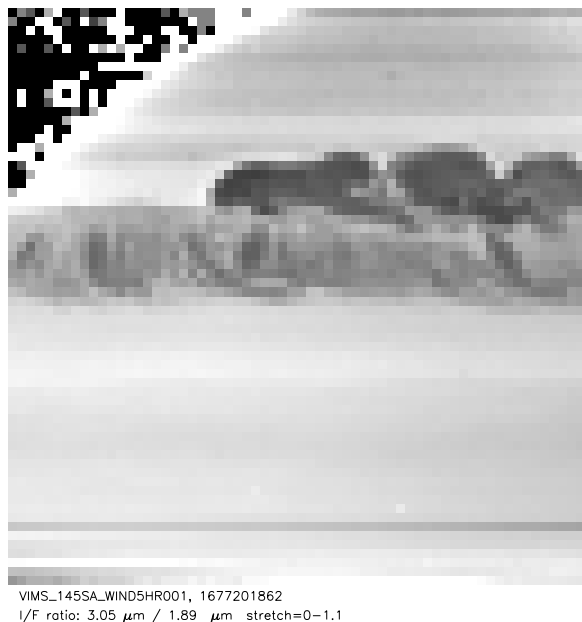


FIG. 4.— VIMS images of I/F ratio between  $3.05 \mu\text{m}$  (numerator) and  $1.89 \mu\text{m}$  (denominator). Absorption by  $\text{NH}_3$  is greatest where the ratio is smallest.

came from PDS example calibrated data cubes, which used a set of wavelengths that was different from those contained in the Jupiter flyby data cube headers. According to McCord et al. (2004), the VIMS wavelength calibration changed since launch by about 12 to 22 nm. Using comparisons with NIMS, they revised the VIMS wavelength calibration to what we believe is in the PDS example calibrated data cubes. These wavelengths are the same as appear in current PDS data cube headers for Saturn (except for the last wavelength). They also match what Cruikshank et al. (2010) refer to as the RC15 wavelength calibration. But, while these wavelengths worked well for the December 2000 Jupiter flyby data, when used with the 2010-2011 Saturn data cubes, they produce conflicts between measurements and model calculations regarding the positions of gaseous absorption bands. To align VIMS spectra with these absorption bands, which are accurately known from line-by-line calculations, re-

quires shifts of the VIMS wavelengths that vary with wavelength. In Fig. 5, we show the results of matching 10 wavelength segments containing different absorption bands. The required shifts are a significant fraction of the 15-nm VIMS resolution, ranging from 12 nm near  $2 \mu\text{m}$  to -4 nm near  $5 \mu\text{m}$ . We found that ramped wavelength shifts lead to better spectral fits than constant segments. The ramp functions we adopted, shown as dot-dashed lines, were adjusted to roughly follow the segment shifts, and to cross zero near  $5 \mu\text{m}$ , where the Fletcher et al. (2011a) analysis of night-side Saturn spectra from 2006 found good agreement between VIMS and model wavelengths. As shown in Section 5.1, fit quality is much worse if unshifted wavelengths are used. This implies that the VIMS instrument changed behavior between the early part of the 2000 Jupiter encounter and operations at Saturn in 2010-2011, by almost as much as the change from pre-launch to the time of the Jupiter approach. Whether the change in instrument temperatures between these two time periods could have been a factor remains to be determined.

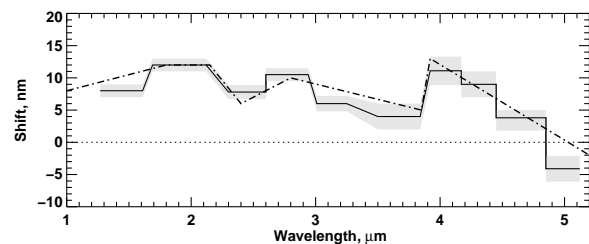


FIG. 5.— VIMS wavelength shifts obtained from matching individual spectral bands within 10 segments (solid stair-step with gray error bands), and adopted ramp shifts (dot-dashed lines) that provide improved matches to complete spectra.

### 3.4. Image processing and navigation

VIMS image cubes were processed using the pipeline processing code downloaded from the Planetary Data System, described by McCord et al. (2004). To navigate the images, we extracted spacecraft and target body states, and instrument pointing information from the in-

dex.tab files contained in the PDS archive volumes. The sun to target distance was retrieved from Cassini NAIF SP kernel files, bypassing the VIMS pipeline code, which used a fixed distance (9.033 AU). These data allow accurate transformation between image coordinates and planet coordinates using SPICE toolkit software (Acton 1996). We processed the VIMS data cube up through the “specific energy” product stage using pipeline software, and then computed the I/F using the correct sun-target distance and the solar spectrum provided in the PDS volumes. The VIMS calibration uncertainty is at least as large as the near-IR solar spectral irradiance uncertainty of  $\sim 3\%$ - $5\%$  (Colina et al. 1996). It appears to be less than 10% uncertain, based on window-region comparisons made by Sromovsky and Fry (2010b) with independent spectra of Jupiter.

### 3.5. VIMS noise characteristics.

For most applications at moderate signal levels, the random noise level of VIMS is very small, nominally less than 1 DN. Sromovsky and Fry (2010b) tried to better characterize the noise by comparing spectra in cubes that imaged the same region of Jupiter with as small a time difference as possible. They found measurements in the same channel to be within about 1.2 DN RMS for a single measurement, even for signal levels up to 2000 DN or more. However, at signals 100 times smaller, as found near  $2.3\ \mu\text{m}$ , Sromovsky and Fry (2010b) found a much larger fractional noise, which can be characterized as an I/F offset noise, which they crudely estimated as  $\sim 5 \times 10^{-4}$  from the on-disk spectra. Other possible sources of uncertainty, though not strictly random noise, are scattered light inside the spectrometer, wavelength errors, line-spread uncertainties, and wavelength-dependent absolute calibration errors.

## 4. RADIATION TRANSFER CALCULATIONS

### 4.1. Atmospheric structure and composition

The assumed composition of the atmosphere as a function of pressure is displayed in Fig. 6. We used the Lindal et al. (1985) temperature structure between 0.2 mb and 1.3 bars and dry adiabatic extrapolation to approximate the structure at deeper levels. Lindal et al. (1985) used a  $\text{He}/\text{H}_2$  ratio of 0.06/0.94 in deriving their profile, and noted that the profile could be scaled to account for a different  $\text{He}/\text{H}_2$  ratio. We used the revised ratio of  $0.135 \pm 0.025$  due to Conrath and Gautier (2000), but did not scale the Lindal et al. thermal profile because that would result in disagreement with the thermal emission spectrum. The Conrath and Gautier (2000) revision was motivated by a disagreement between the pre-Galileo  $\text{He}/\text{H}_2$  ratio for Jupiter and the accurate in situ measurements by the Galileo Probe. The pre-Galileo result was based on a combined analysis of IRIS spectra and the Voyager-measured radio occultation refractivity profile. In an attempt to avoid whatever error had occurred in that Jupiter analysis, Conrath and Gautier based their Saturn revision entirely on Voyager IRIS observations. A lower value of 0.08 was given by Fouchet et al. (2009) based on Cassini CIRS spectra and Cassini radio occultations analyzed by Gautier et al. (2006). Fortunately, these uncertainties in the  $\text{He}/\text{H}_2$  ratio have little effect on our analysis. As long as the derived thermal profiles remain in agreement with the thermal emission spectra,

which is true for all of these results, we found that our derived cloud model parameters are not very sensitive to the  $\text{He}/\text{H}_2$  ratio. Test cases for ratios from 0.06 to 0.135 show that the derived cloud parameters don’t change more than their uncertainty limits. After trying a variety of values for the  $\text{CH}_4$  volume mixing ratio (VMR), we found the best fits were generally obtained with the Fletcher et al. (2009b) value  $(4.7 \pm 0.2) \times 10^{-3}$ , which corresponds to a  $\text{CH}_4/\text{H}_2$  ratio of  $5.3 \times 10^{-3}$ . For  $\text{CH}_3\text{D}$  we also used the Fletcher et al. (2009b) VMR value of  $3 \times 10^{-7}$ . The most important variable gas is  $\text{PH}_3$  and its vertical profile needs to be adjusted to fit VIMS spectra. Fletcher et al. (2009a) has shown that  $\text{PH}_3$  is enhanced over the equator and depleted over belts and within hot cyclonic polar vortices. We found that a reasonably effective parameterization was a fixed deep mixing ratio and an adjustable scale height defining its rate of decrease for pressures less than about 600 mb. Our best fits outside the storm region were obtained with a deep mixing ratio of  $6.4 \times 10^{-6}$ , which is the global mean value of Fletcher et al. (2009a), and a scale height of 37.5% of the pressure scale height. Inside the storm region better fits were obtained with a more extended  $\text{PH}_3$  profile using the same deep mixing ratio and 50% of the pressure scale height. The greater scale height within the storm is consistent with increased upward transport of  $\text{PH}_3$ , as expected in regions of strong convection. We used the  $\text{NH}_3$  profile given by Prinn et al. (1984), which has a constant deep mixing ratio of  $2.05 \times 10^{-4}$ , based on Courtin et al. (1984). More recent VLA results include a value of  $(4.8 \pm 1) \times 10^{-4}$  by Briggs and Sackett (1989) and some evidence for depletion of  $\text{NH}_3$  in the 2-4 bar region, which they interpret as evidence for an  $\text{NH}_4\text{SH}$  cloud and  $\text{H}_2\text{S}$  vapor. Arsine has a noticeable effect on the VIMS spectra near  $5\ \mu\text{m}$ , which is where ammonia gas also plays a relatively minor role. Although  $\text{NH}_3$  absorbs over a wide wavelength range, its effects are largely shielded by overlying cloud opacity. It does however have a minor influence in blocking some of the thermal radiation at wavelengths beyond  $4.6\ \mu\text{m}$ .

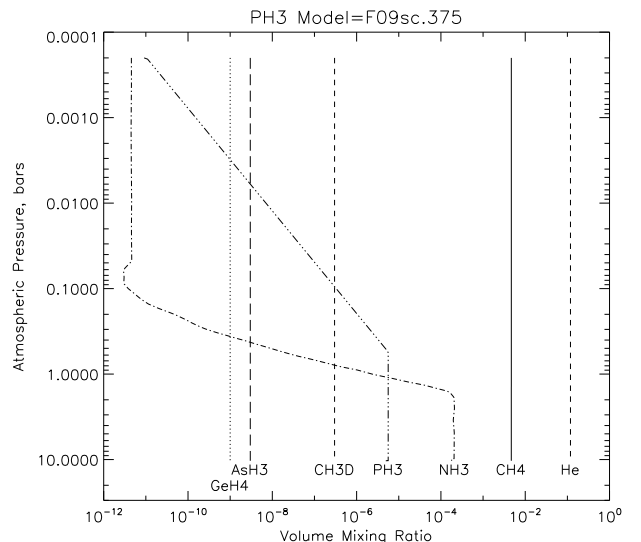


FIG. 6.— Assumed volume mixing ratios of spectroscopically important gases in the atmosphere of Saturn. See text for references.

#### 4.2. Gas absorption models

Because we wanted our correlated-k methane absorption models to be based on line-by-line calculations, we limited our spectral analysis to wavelengths greater than  $1.268\ \mu\text{m}$ . Recent advances in measuring line spectra (Campargue et al. 2012) have improved line-by-line calculations so much that for  $\lambda > 1.268\ \mu\text{m}$  they are now likely more accurate than band models (see Sromovsky et al. (2012) for comparisons and correlated-k models). We used the same line data for computing  $\text{CH}_3\text{D}$  absorption models. For  $\text{NH}_3$  we used the combined correlated-k absorption model described by Sromovsky and Fry (2010a), which is based primarily on the Goody-Lorentz band model of Bowles et al. (2008). To model phosphine ( $\text{PH}_3$ ) absorption we used our own exponential sum approximations based on the line data of Butler et al. (2006) in the  $2.8\text{--}3.1\ \mu\text{m}$  region and on the Rothman et al. (2009) HITRAN 2008 line data in the  $4.1\text{--}5.1\ \mu\text{m}$  region. Our model of  $\text{AsH}_3$  absorption is based on line data from Tarrago (1996) (via G. Bjoraker, via B. Bézard, personal communication). Where  $\text{CH}_4$  and  $\text{PH}_3$  gas absorptions overlap we compute opacities for 100 combinations of 10  $\text{CH}_4$  terms by 10  $\text{PH}_3$  terms and then sort and refit to a 10-term weighted sum, following the suggestion of Lacis and Oinas (1991). We do the same with all other gas overlaps in succession, which reduces all gas absorptions to ten-term exponential sum models at all wavelengths, even in regions with overlap of several gases.

Collision-induced absorption (CIA) for  $\text{H}_2$  and  $\text{H}_2\text{--He}$  was calculated using programs downloaded from the Atmospheres Node of the Planetary Data System, which are documented by Borysow (1991, 1993) for the  $\text{H}_2\text{--H}_2$  fundamental band, Zheng and Borysow (1995) for the first  $\text{H}_2\text{--H}_2$  overtone band, and by Borysow (1992) for  $\text{H}_2\text{--He}$  bands. Although these programs and/or tables generally provide coefficients only for normal and equilibrium hydrogen, absorption for any para fraction can be derived by appropriate linear combinations of these values (Birnbaum et al. 1996). We used equilibrium hydrogen generally and made test calculations with normal hydrogen to assure ourselves that our conclusions were not sensitive to the ortho/para ratio.

#### 4.3. Multiple scattering methods

For multiple scattering calculations we make use of a modification of the doubling and adding code described by Sromovsky (2005a,b). The modification is to remove the Raman source term, which is not needed at near-IR wavelengths, and restore the original blackbody emission source term (Evans and Stephens 1991) to handle the  $5\text{--}\mu\text{m}$  region of the spectrum. We used a grid of 44 pressure levels from 0.5 mb to 10 bars, distributed roughly in equal log increments, except that additional layers are introduced where cloud layers are inserted. As a function of wavelength we stop adding layers after the one-way vertical gas optical depth exceeds six. To model the medium phase angle VIMS observations we used 16 quadrature points in both zenith angle and azimuth. We followed Sromovsky and Fry (2010a,b) in modeling coated-sphere particle scattering using code originated by Toon and Ackerman (1981). We approximated the line-spread function of the VIMS instrument as a Gaussian of  $\text{FWHM} = 0.015\ \mu\text{m}$ , then collected all

the opacity values within  $\pm\text{FWHM}$  of the sample wavelength, weighted those according to the relative amplitude of the line-spread function, then sorted and refit to ten terms again. A special treatment is required in the  $2.9\text{--}3.0\ \mu\text{m}$  region where  $\text{NH}_3$  cloud particles have very sharp absorption features. In this region model calculations were made at  $5\text{-cm}^{-1}$  intervals (the maximum sampling frequency of our correlated-k models) and subsequently smoothed to VIMS resolution.

#### 4.4. Fitting cloud models to observations

Our cloud models usually included both vertically extended layers, where layer boundaries could be constrained by the observations, and compact layers, where the vertical extent of cloud layers could not be constrained. In some cases we evaluate both compact and vertically extended models, often finding that both can work for layers that are weakly constrained. For models where the number of adjustable parameters is relatively small, parameters were adjusted to minimize  $\chi^2$  using a form of the Levenberg-Marquardt algorithm, as described by Press et al. (1992). In most cases, model complexity is too large to reach automated convergence of all parameters in a practical time period (or ever). To reduce the scale of the fitting problem and increase algorithm stability, we use constraining assumptions for a subset of the parameters, which usually cannot be assigned reliable uncertainty estimates. It is important to note that formal uncertainties in the remaining fitted parameters are only valid within the context of the constraining assumptions and cannot be treated as absolute uncertainties.

To speed the fitting process we reduce the total number of spectral comparisons to a set of 48 wavelengths that sample key spectral features and a wide range of gaseous absorption strengths. After fitting adjustable parameters to minimize  $\chi^2$  for the sampled points, we then compute a complete spectrum for more detailed comparisons. To test for the presence of bias due to the specific wavelengths sampled in constraining our fits, we did a fit to the Location 4 spectrum with the complete set of 225 uniformly spaced wavelengths as constraints. The two resulting sets of fit parameters agreed within their uncertainties, indicating no significant bias.

#### 4.5. Estimating uncertainties in derived model parameters

The constraining properties of the observations depend on the nature of measurement errors as well as on the errors in the modeling of atmospheric opacity. As previously noted, the VIMS random I/F measurement errors in a given wavelength channel are negligible except at very low signal levels. Systematic errors are more of a concern, both in absolute calibration and in the wavelength scale, which can itself result in I/F errors when comparing to models at slightly incorrect wavelengths. A more important error source, which is not strictly random, but can vary from wavelength to wavelength, is the uncertainty in radiation transfer modeling due to the uncertainty in absorption coefficient models. The transmission curves on which previous methane opacity models were based had an assumed error of 0.05 (Irwin et al. 2006). Although not well characterized, the correlated-k

models derived from line-by-line calculations also produce uncertainties.

To try to account for these effects we used the following procedure. Initial model fits are used to establish a rough characterization of the vertical opacity structure of the atmosphere. We then calculate model spectra for the rough model, and for two perturbations: (1) optical depths offset by 0.01 and (2) optical depths increased by 10%. The resulting I/F differences are root sum squared with I/F errors due to wavelength uncertainties, and with an I/F offset uncertainty of  $5 \times 10^{-4}$  and a measurement/relative calibration uncertainty assumed to be 1%. The I/F error associated with wavelength uncertainty is calculated from the derivative of the I/F spectrum with respect to wavelength times an estimated wavelength uncertainty of  $0.002 \mu\text{m}$ , which is  $1/8$  of a VIMS line width. In some cases we assume a simpler uncertainty model, which is not cloud model dependent, but is characterized by an I/F offset uncertainty of 0.002 and a fractional I/F uncertainty of 10%. The expected  $\chi^2$  value for the best fit is equal to the number of degrees of freedom  $N_F$  (number of points of comparison minus the number of adjusted parameters) and the expected uncertainty in the value is equal to  $\sqrt{2N_F}$  (Rice 1995). However, both error models result in minimum  $\chi^2$  values several times  $N_F$ . This means that either our error estimates are too low, or our physical models of the clouds are incomplete. There are many reasons for the latter to be true, including not-accounted-for effects of non-spherical particles, multi-coated particles (more than two compositional layers), and heterogeneous structures, as well as more complex vertical distributions. To approximately correct for bad error estimates and incomplete physics, we rescaled our  $\chi^2$  values by the factor  $N_F/\chi^2_{MIN}$  before finding confidence limits. Because higher than expected  $\chi^2$  values are probably not simply due to bad error estimates, this procedure is not entirely valid, but is clearly better than making no adjustment.

## 5. MODELING CLOUD STRUCTURE OUTSIDE THE STORM REGIONS.

### 5.1. Sample fits using a simplified cloud structure

Near IR spectra outside the storm regions can be very well fit by relatively simple cloud structures, which are similar to those used successfully to fit spectra in the CCD range from  $0.3$  to  $1 \mu\text{m}$  (Muñoz et al. 2004; Karkoschka and Tomasko 2005; Pérez-Hoyos et al. 2005). These structures contain a vertically diffuse stratospheric haze, an optically thick and physically thick main cloud layer, which requires visible and UV absorption, but can fit near IR spectra with conservative cloud particles, and a deeper layer, to which most wavelengths have little sensitivity, but which can be constrained by the thermal emission that can be sensed in the  $5\text{-}\mu\text{m}$  region. Fits of such a model structure to the VIMS spectra from all non-storm locations identified in Figs. 2 are summarized in Table 1, where parameter values, uncertainties, and  $\chi^2$  values are all derived from the subset of 48 spectral samples discussed previously. In all these fits we characterized the deep cloud as physically compact, but optically thick (arbitrarily set to  $\tau = 30$ ) and absorbing (set to  $\varpi=0.9$  to provide adequate blocking of thermal emission). The only adjustable parameter of this

layer was its effective pressure. As will be shown in the following, other deep cloud options could also be made to work. Cloud particles in the main haze layer (generally between 120 and 700 mb) were treated as Mie particles with refractive index  $n=1.4+0i$ . We fit the upper and lower pressures of this layer and its optical depth at  $2 \mu\text{m}$ , and within the boundaries of this layer we assumed a vertical scale height equal to the gas scale height. Because our  $\chi^2$  values are several times the expected value (the number of degrees of freedom), it is clear that either our model lacks needed physics or our measurement error estimate is too small, by a factor of  $\sqrt{\chi^2_{MIN}/N_F}$ , or some of both. If we assume that our error estimate is the problem, then we need to multiply our standard parameter uncertainty estimate (the change needed to produce  $\Delta\chi^2 = 1$ ) by the same factor of  $\sqrt{\chi^2_{MIN}/N_F}$ . Error estimates in Table 1 have this correction applied.

The complete best-fit model spectrum for location 4 is displayed in Fig. 7. We also evaluated the fit quality of this spectrum using  $\chi^2$  computed for all measured points, assuming a simplistic random error model with a reflectivity (I/F) fractional uncertainty of 0.1 and an offset uncertainty of 0.002, which provides more of a relative than absolute judgment of fit quality. This provides a convenient way to compare full resolution versions of the best-fit model spectra. Two  $\chi^2$  values are shown in the legend of Fig. 7: the one labeled  $\chi^2/N(\text{TOT})$  is computed for  $1.268\text{-}5.15 \mu\text{m}$  wavelength range, and the one labeled  $\chi^2/N(\text{ABS})$  is computed for the  $2.65\text{-}3.2 \mu\text{m}$  range where particulate absorption features can be prominent (in the storm region). All are computed with respect to the wavelength-shifted spectrum. If computed relative to an unshifted spectrum the  $\chi^2/N(\text{ABS})$  increases from 0.26 to 2.3 and  $\chi^2/N(\text{TOT})$  increases from 0.98 to 3.8. This is a dramatic change that clearly confirms the need for wavelength corrections. Although the fit quality for this model is very high, the model is not unique. A deep cloud that is vertically extended, with a constant optical depth per unit pressure, can fit just as well, provided it contains some absorption that increases with wavelength.

### 5.2. Sensitivity of model spectrum to model parameters

Figure 7 also displays the effect of removing each model layer one at a time, and also the effect of removing various gases from the atmospheric absorption model. Next to methane, phosphine has the most significant effect on the spectrum. Hydrogen CIA is next most significant, but limited to wavelengths from  $2$  to  $2.2 \mu\text{m}$ . The stratospheric haze provides the baseline I/F in the darkest parts of the spectrum. However, because of the anomalously large I/F values measured by VIMS at very small I/F levels (Sromovsky and Fry 2010b), and the small reflectivity of the small stratospheric haze particles at near IR wavelengths, what can be learned about that haze from the VIMS observations is rather limited. We found that a Mie particle radius of  $0.1 \mu\text{m}$  or a Henyey-Greenstein scatterer with wavelength dependence of  $\lambda^{-3.5}$ , a pressure level of 2 mb, and an adjustable optical depth provides a suitable model. But this is not a very realistic physical model of the stratospheric haze. Extending the haze downward as prior CCD-based models have done, does not improve the accuracy of fits here,



probably due to the offset errors of the VIMS instrument.

### 5.3. Alternate vertical distributions

The variety of vertical distributions that can fit the near IR spectra is similar to the variety that have been used to fit the visible spectra, as illustrated in Fig. 8, where we compare our fits to the non-storm spectrum from location 4 in Fig. 2 to models of Pérez-Hoyos et al. (2005) and Karkoschka and Tomasko (2005) applicable to similar latitudes, but different time periods. The disagreements are not surprising, given the secular variation that might have occurred between the relevant observing times. We tried both broadly diffuse vertical distributions suggested by Karkoschka and Tomasko (2005) and the more compact models used by Pérez-Hoyos et al. (2005). We found reasonably good fits were possible with both types of models, even to the  $5\text{-}\mu\text{m}$  region. By making use of thermal wavelengths ( $\lambda > 4.8\text{ }\mu\text{m}$ ), we were able to place better constraints on the deep cloud structure than were the previously cited authors, though here again there is not a clear distinction that can be made between compact and diffuse models. If we assume that the upper cloud has a real index of 1.4, and that the deep cloud is nearly conservative ( $\varpi=0.98$ ) and compact (Model B in Fig. 8), then we find that the cloud needs to reside near 3.3 bars and have a high optical depth ( $\tau \sim 150$ ). But if the cloud is more strongly absorbing ( $\varpi=0.9$  as in Model C in Fig. 8), then the optical depth requirement is greatly reduced ( $\tau \sim 30$ ) while the pressure remains essentially unchanged. In all these cases the main haze layer visible from above was assumed to have a refractive real index of 1.4, to be uniformly mixed with gas, and to have adjustable top and bottom pressures, which reached typical values of 178 mb and 780 mb respectively, while the optical depth did not deviate much from 6.8 at  $2\text{ }\mu\text{m}$ . Although the compact lower cloud models with a separated upper tropospheric layer (extending from 178 mb to 780 mb) provided the best fits (B and C in Fig. 8), we were also able to get reasonable fits with a semi-infinite diffuse cloud extending downward from 178 mb, using an opacity of 11 optical depths/bar (A in Fig. 8), with a real index of 1.4 and an imaginary index linearly increasing from 0.001 at  $1\text{ }\mu\text{m}$  to 0.003 at  $5.5\text{ }\mu\text{m}$ . This latter model is similar to that used by Karkoschka and Tomasko (2005). Perhaps the most significant deviation is that our VIMS-based fits for the stratospheric haze layer are not consistent with that haze extending down to 100-300 mb, as found by prior fits. We believe that this disagreement arises from an artifact of the VIMS instrument in which very low I/F values are too high, as explained in Section 3.2.

### 5.4. Latitudinal variations in non-storm regions

Fits to spectra from all non-storm locations identified in Fig. 2 and summarized in Table 1 are graphically displayed in Fig. 9. In these non-storm fits, which sampled latitudes from  $20^\circ\text{ N}$  to  $48^\circ\text{ N}$ , there is a trend for the main upper tropospheric haze layer towards smaller particles and smaller optical depths with increased latitude. In these fits there is no significant variation in the effective height of the thermal blocking layer. The significantly worse fit to the location 6 spectrum, which is from the near equatorial region, arises mostly from the

low model I/F in the  $1.5\text{-}1.6\text{ }\mu\text{m}$  continuum region, which might be due to a small amount of unaccounted-for absorption in the main cloud later in that broad equatorial band. Note that these fits exclude the latitude region between  $22^\circ\text{ N}$  and  $30^\circ\text{ N}$ , where there has been a strong storm influence, as indicated by the temporal changes evident in Fig. 1. Analyzing the character of that disturbed region is left for future work.

### 5.5. Composition of the main cloud layer in non-storm regions

None of the fits to the non-storm regions required any unusual absorption in the vicinity of  $3\text{ }\mu\text{m}$ , where  $\text{NH}_3$ ,  $\text{N}_2\text{H}_4$ , and  $\text{NH}_4\text{SH}$  have substantial absorption. According to Fig. 4, there is a wide spread lack of  $3\text{-}\mu\text{m}$  particulate absorption in regions not affected by the storm. It thus appears that the main upper cloud layers outside the storm-affected regions are not composed primarily of these materials. This is a well known mystery that remains to be definitively solved. It is quite amazing that the main cloud layer on Saturn that is accessible to remote observations, which is of high optical depth and thus represents a significant cloud mass, is apparently made of materials that have no detectable near-IR spectral signatures and thus do not seem to contain any significant contributions from the main condensable gases on Saturn.

Explanations for how ammonia could really be the dominant condensable in the main haze layer, even though it has not been detectable outside of storm regions, have focused on three possible concealment mechanisms: (1) large particle sizes, (2) non-spherical particle shape effects, or (3) foreign coating or contamination. West et al. (2009) reviewed these explanations and rejected them all, noting that a foreign contaminant would have to be the dominant cloud mass to be effective at suppressing the  $\text{NH}_3$  signatures. Our calculations with composite particles are consistent with the conclusions of West et al. and our inferred particle sizes are also too small ( $\sim 1\text{ }\mu\text{m}$  or less) to support (1).

The leading candidate for the upper tropospheric haze according to Fouchet et al. (2009) is diphosphine ( $\text{P}_2\text{H}_4$ ), which does not absorb much at  $3\text{ }\mu\text{m}$ , but has a distinctive double absorption peak signature near  $4.3\text{ }\mu\text{m}$  and another at  $6\text{ }\mu\text{m}$  (Nixon 1956). If the  $4.3\text{-}\mu\text{m}$  peaks of diphosphine have roughly the same strength as the double absorption peak of hydrazine ( $\text{N}_2\text{H}_4$ ), then that signature should be visible even though it is partly obscured by  $\text{PH}_3$  absorption. However, though no such signature is seen either in or out of storm regions, it is premature to completely rule out diphosphine until refractive index measurements allow accurate radiative transfer calculations to be made. We can rule out hydrazine as the major component of the main upper tropospheric haze because its distinctive features would be easily detected, as apparent from the discussion in the following sections.

## 6. MODELING THE $3\text{-}\mu\text{m}$ ABSORPTION IN STORM CLOUD SPECTRA.

We first consider what compositions might be plausible, try simple spectral fits using pure substances in a single main cloud layer, evaluate their relative advantages, then consider more complex structures including overlying sub-layers and composite particles.



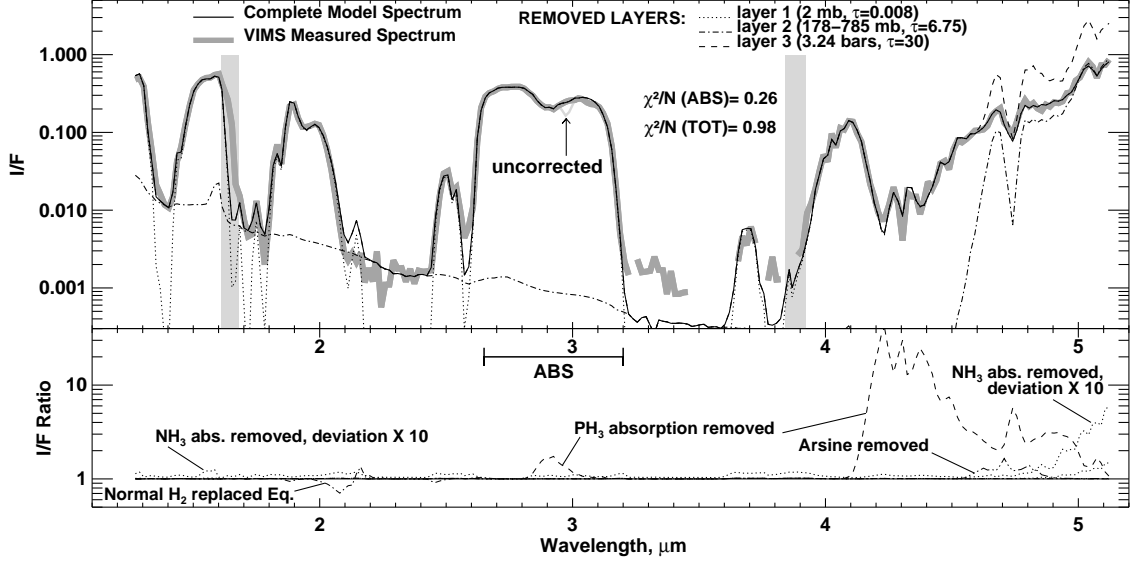


FIG. 7.— Example model spectrum (thin solid curve) fit to the VIMS mid-latitude spectrum (thick gray curve) from location 4 in Fig. 2. The model parameters are given in Table 1. Contributions from each layer can be inferred from the spectral changes produced by removing it. Relative fit quality for the entire spectrum (excluding the two regions indicated by vertical gray bars) is indicated by the  $\chi^2/N$  (TOT) values, and for the  $2.65 \mu\text{m} - 3.2 \mu\text{m}$  region of particulate absorption by  $\chi^2/N$  (ABS) values, where there are 33 points in the ABS region and 223 in total. Sensitivities to gas absorptions by  $\text{NH}_3$  (dotted),  $\text{PH}_3$  (solid),  $\text{AsH}_3$  (double dot-dash) and normal vs. equilibrium  $\text{H}_2$  (dot-dash) are indicated by ratio spectra in the bottom panel (modified model/best-fit model). Greater sensitivity to these gases would be obtained in regions of lower cloud opacity. The importance of thermal emission in constraining deep cloud opacity can be seen from the large I/F increase caused by removal of layer 3. Vertical gray bars indicate where order sorting filter joints cause uncorrected VIMS I/F uncertainties. At the joint near  $2.96 \mu\text{m}$ , the measured spectrum has been corrected for responsivity errors following a procedure described in the text. The thin lighter gray curve shows the original uncorrected spectrum. The good agreement of the corrected spectrum with model calculations in this region attest to the efficacy of the correction.

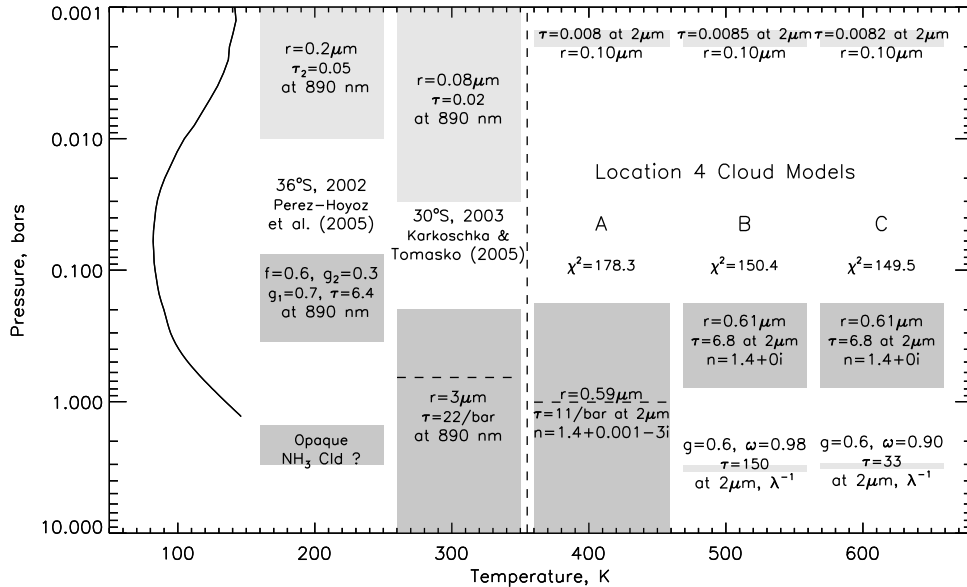


FIG. 8.— Sample cloud structure models for Saturn according to Pérez-Hoyos et al. (2005) and Karkoschka and Tomasko (2005) and, to the right of the vertical dashed line, our model fits to the spectrum from location 4 in Fig. 2. Structure A uses a uniformly mixed single particle type from cloud top to the bottom of the atmosphere, as used by Karkoschka and Tomasko (2005). To provide sufficient absorption of long wavelengths this requires an imaginary index that increases with wavelength. Structures B and C, which are similar to that used by Pérez-Hoyos et al. (2005), differ in the single-scattering albedo assumed for the lower cloud layer. Higher albedo requires larger optical depth to block thermal emissions.  $\chi^2$  values shown are for fits to the 48-wavelength sampled spectra.

### 6.1. Optical properties of candidate cloud materials

Cloud materials expected in Saturn's atmosphere that also absorb light in the  $3\text{-}\mu\text{m}$  region, include  $\text{NH}_3$  ice,  $\text{NH}_4\text{SH}$  (ammonium hydrosulfide), water ice,  $\text{N}_2\text{H}_4$  (hy-

drazine), and possibly solid  $\text{P}_2\text{H}_4$  (diphosphine), although it appears that the latter has only very weak bands in this region (Frankiss 1968). Refractive index plots for these materials (except diphosphine, which has not been characterized) are shown in Fig. 10. Among

TABLE 1  
CLOUD MODEL PARAMETER FITS FOR FEBRUARY 2011 NON-STORM SPECTRA.

Parameter	Location 3	Location 4	Location 5	Location 6
Planetocentric Lat., °	36.78	34.41	47.52	19.00
Planetographic Lat., °	42.57	40.10	53.32	22.94
East Long., °	-116.09	-115.89	-110.63	-102.90
Stratospheric haze $\tau \times 10^3$	$8.6 \pm 0.9$	$8.6 \pm 0.8$	$7.5 \pm 0.7$	$15.0 \pm 1.8$
Main haze Ptop, mb	$143 \pm 11$	$178 \pm 12$	$132 \pm 11$	$111 \pm 12$
Main haze Pbottom, mb	$844 \pm 110$	$785 \pm 82$	$577 \pm 76$	$633 \pm 73$
Main haze $\tau$	$6.53 \pm 0.81$	$6.75 \pm 0.66$	$3.48 \pm 0.36$	$8.57 \pm 0.83$
Main haze part. radius, $\mu\text{m}$	$0.55 \pm 0.04$	$0.61 \pm 0.05$	$0.43 \pm 0.02$	$0.71 \pm 0.07$
Deep cloud Pbase, bar	$2.98 \pm 0.11$	$3.25 \pm 0.07$	$2.68 \pm 0.15$	$2.99 \pm 0.11$
$\chi^2$	204.08	149.87	169.30	430.19

Uncertainties are  $1\text{-}\sigma$  values after adjustment for excess  $\chi^2$  minimum, as described in text.  $\chi^2$  values are for fits to the 48-wavelength sampled spectra. Locations refer to Fig. 2.

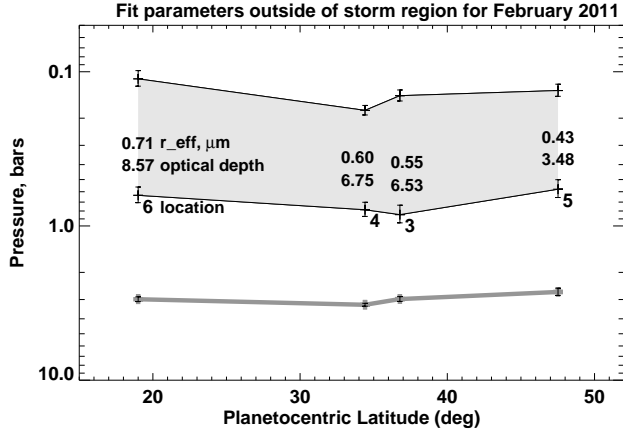


FIG. 9.— Pressure boundaries of main cloud layer and effective pressure of thermal barrier cloud vs latitude, with annotated values of location, optical depth, and particle size. Locations refer to Fig. 2.

the more plausible storm particle components,  $\text{NH}_3$  ice has the strongest and sharpest absorption at  $2\text{ }\mu\text{m}$  (the  $2.25\text{ }\mu\text{m}$  absorption feature would not be visible due to overlying gas absorption). Hydrazine, which is not expected to be very abundant on Saturn, has a pair of strong absorption peaks between 3 and  $3.2\text{ }\mu\text{m}$ , which would be very apparent unless cloud particles were very large. Though diphosphine, which is expected to be more abundant on Saturn (Fouchet et al. 2009), could plausibly also contribute to the storm particle mix, we have no evidence in the VIMS storm spectra of its distinctive double absorption peaks near  $4.35\text{ }\mu\text{m}$ , and no refractive index measurements that would allow us to include it in quantitative radiative transfer models.  $\text{NH}_4\text{SH}$  has an absorption that is roughly comparable to that of  $\text{NH}_3$  at  $3\text{ }\mu\text{m}$ , but lacks a sharp spectral feature and continues to increase beyond  $3.1\text{ }\mu\text{m}$  while  $\text{NH}_3$  absorption drops significantly.

There is some disagreement about the detailed refractive index variation with wavelength for  $\text{NH}_3$ . A comparison of results from Martonchik et al. (1984) and from Roux et al. (1979) is provided in Fig. 11. Because Roux et al. (1979) provides better spectral resolution in

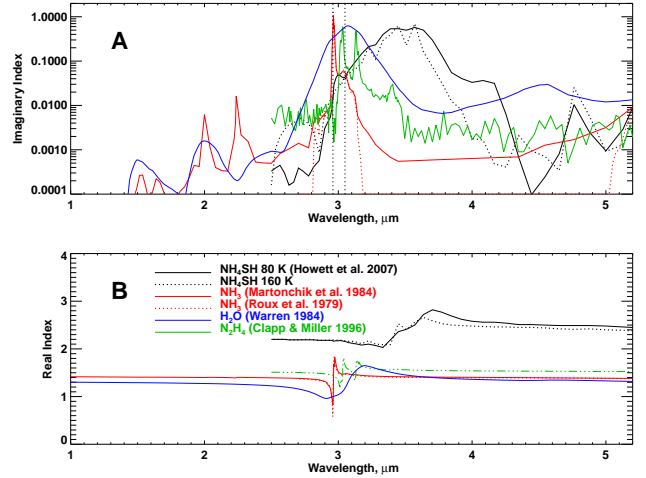


FIG. 10.— Imaginary (A) and real (B) components of the refractive index vs. wavelength for candidate  $3\text{-}\mu\text{m}$  absorbers, including  $\text{H}_2\text{O}$  results of Warren (1984),  $\text{NH}_3$  results of Roux et al. (1979) and Martonchik et al. (1984),  $\text{NH}_4\text{SH}$  results of Howett et al. (2007), and  $\text{N}_2\text{H}_4$  results of Clapp and Miller (1996). Vertical dotted lines at  $2.96$  and  $3.05\text{ }\mu\text{m}$  indicate approximate locations of  $\text{NH}_3$  absorption features.

the  $2.7\text{-}3.1\text{ }\mu\text{m}$  region and provides no information below  $2.8\text{ }\mu\text{m}$ , we initially used Martonchik et al. (1984) for  $\lambda < 2.8\text{ }\mu\text{m}$  and Roux et al. (1979) for longer wavelengths. These two references also disagree on the level of absorption near  $5\text{ }\mu\text{m}$ . We later used a different blend in which we used Martonchik et al. (1984) everywhere except between  $2.88\text{ }\mu\text{m}$  and  $3.14\text{ }\mu\text{m}$ , where Roux et al. (1979) is used. This provides improved fit quality for some models. There is also evidence for small variations of optical properties with temperature (Sill et al. 1980), which we cannot account for and thus are forced to ignore.

## 6.2. Initial spectral fits with pure particles

The five substances we considered in preliminary calculations with single-composition particles are these: (1) conservative substance with refractive index  $n=1.4+0i$ , (2)  $\text{NH}_3$ , (3)  $\text{NH}_4\text{SH}$ , (4)  $\text{N}_2\text{H}_4$ , and (5) water ice. As indicated in Fig. 10, substances 2-5 all have significant

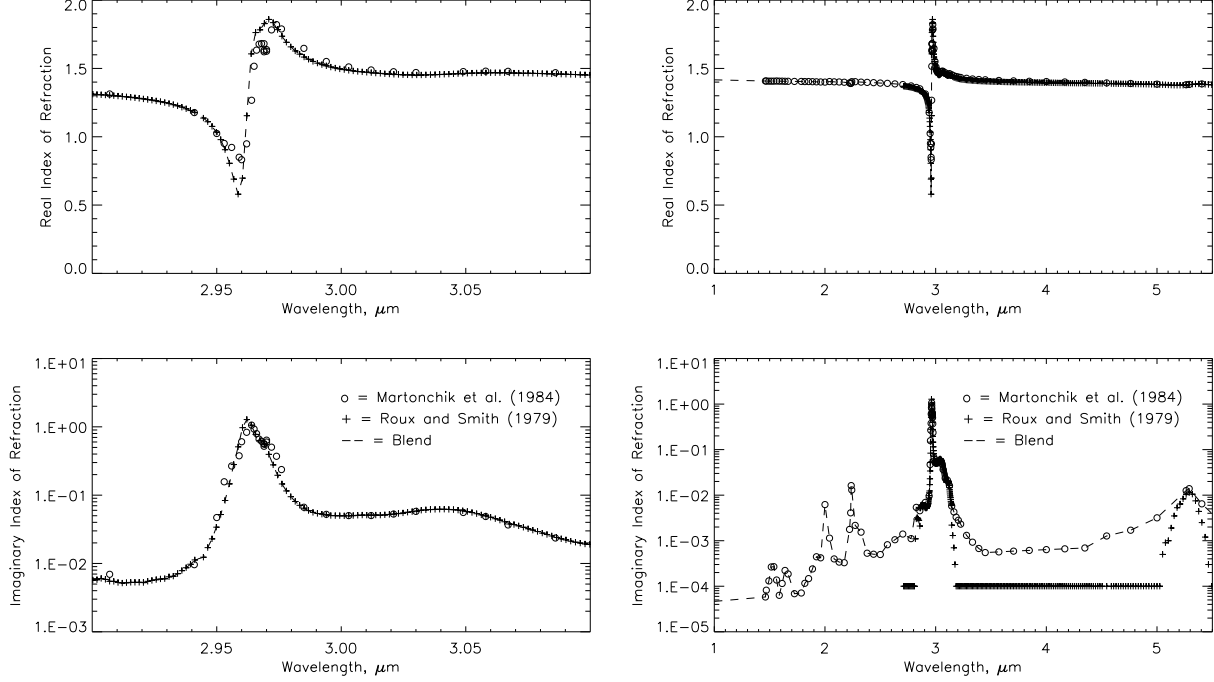


FIG. 11.— Comparison of Martonchik et al. (1984) and Roux et al. (1979) measurements of the refractive index of  $\text{NH}_3$ . Our second blended version (dashed curve), uses the former everywhere except between  $2.88\ \mu\text{m}$  and  $3.14\ \mu\text{m}$ , where the latter is used. Roux et al. (1979) provides a better match to VIMS observations near  $2.9\ \mu\text{m}$ , while Martonchik et al. (1984) provides a better match near  $5\ \mu\text{m}$ .

absorption in the  $3\text{-}\mu\text{m}$  region. The question we are trying to answer is which substance is dominant, if any, and is there evidence of contributions from more than one substance? The great depth of vertical convection suggested by numerical models of the dynamics of this feature (Hueso and Sánchez-Lavega 2004) makes it plausible to consider that even water ice might reach levels of the main cloud layer. Intense lightning strikes inferred from static electric discharge (SED) events measured by the Cassini Radio and Plasma Wave instrument (RPWS) occurred mainly near the head of the storm and indicate that this is a deep convective storm area energized by latent heat of water condensation in the 10-20 bar level. Other lightning strikes seen optically by the ISS instrument confirm their vertical location 125-250 km below the upper cloud layer (Dyudina et al. 2010).

To gain a better understanding of how various plausible particle constituents might contribute to the  $3\text{-}\mu\text{m}$  absorption feature, we first try to fit the storm spectra using pure substances in a single middle cloud layer, leaving for later the issue of possible composite particles and/or multiple layers of different composition. We assumed that the middle layer was composed of pure spherical particles, then adjusted the optical depth, particle size, and top and bottom pressures to optimize fits for the region from  $1.268\ \mu\text{m}$  to  $5.15\ \mu\text{m}$ , but ignoring the region from  $2.65\ \mu\text{m}$  to  $3.2\ \mu\text{m}$ , where particulate absorption is most prominent, as well as ignoring the two narrow regions indicated in Fig. 12, where VIMS measurements have large uncertainties (described in Section 3.1). That allows the vertical structure of the aerosols to be primarily constrained by methane gas absorption and not much affected by particulate absorption. We then compared the model spectra with measured spectra in the  $2.65\ \mu\text{m}$  -  $3.2\ \mu\text{m}$  region to determine which provided the best

compositional match.

The fits for the five pure substances are displayed in Fig. 12A. The fit parameters and fit quality are summarized in Tables 2 and 3. We evaluate the overall fit using  $\chi^2$  computed as described for the non-storm regions. The conservative particles with  $n=1.4$  (Fig. 12A) provide a reasonably good spectral fit at all wavelengths except in the  $3\text{-}\mu\text{m}$  region, where the model has a small atmospheric absorption due to phosphine and the measurements require a much larger absorption over a broader range that must be due to cloud particles. The phosphine absorption is particularly small here because the cloud layer containing these particles is relatively high (140-550 mb) and optically thick ( $\tau=9$  at  $2\ \mu\text{m}$ ). The residual absorption (colored yellow in Fig. 12A), which is the difference between the conservative model (red curve) and the measured VIMS spectrum (thick gray curve in Fig. 12), thus must be provided predominantly by particle absorption, and entirely so between  $3.05$  and  $3.1\ \mu\text{m}$ . This also shows that the particle absorption is significant.

The ammonia spectrum provides by far the best match to the measured spectrum of the storm head, yielding a  $\chi^2$  value in the absorbing region that is 3.5 times better (smaller) than that of the next best fit. While ammonia particles provide the best fit among these simplistic single-component models, the resulting model spectrum still contains substantial differences from the VIMS measured spectrum, especially the sharp ammonia ice absorption feature near  $2.96\ \mu\text{m}$ , but also the excess brightness near  $3.1\ \mu\text{m}$ . The model spectrum also has a small dip at  $2\ \mu\text{m}$ , where  $\text{NH}_3$  has another sharp, but much weaker, absorption feature, while a corresponding dip is not seen in the measured spectrum.

Turning to the option of pure  $\text{NH}_4\text{SH}$  particles (green curve in Fig. 12A), we see that the overall fit is better

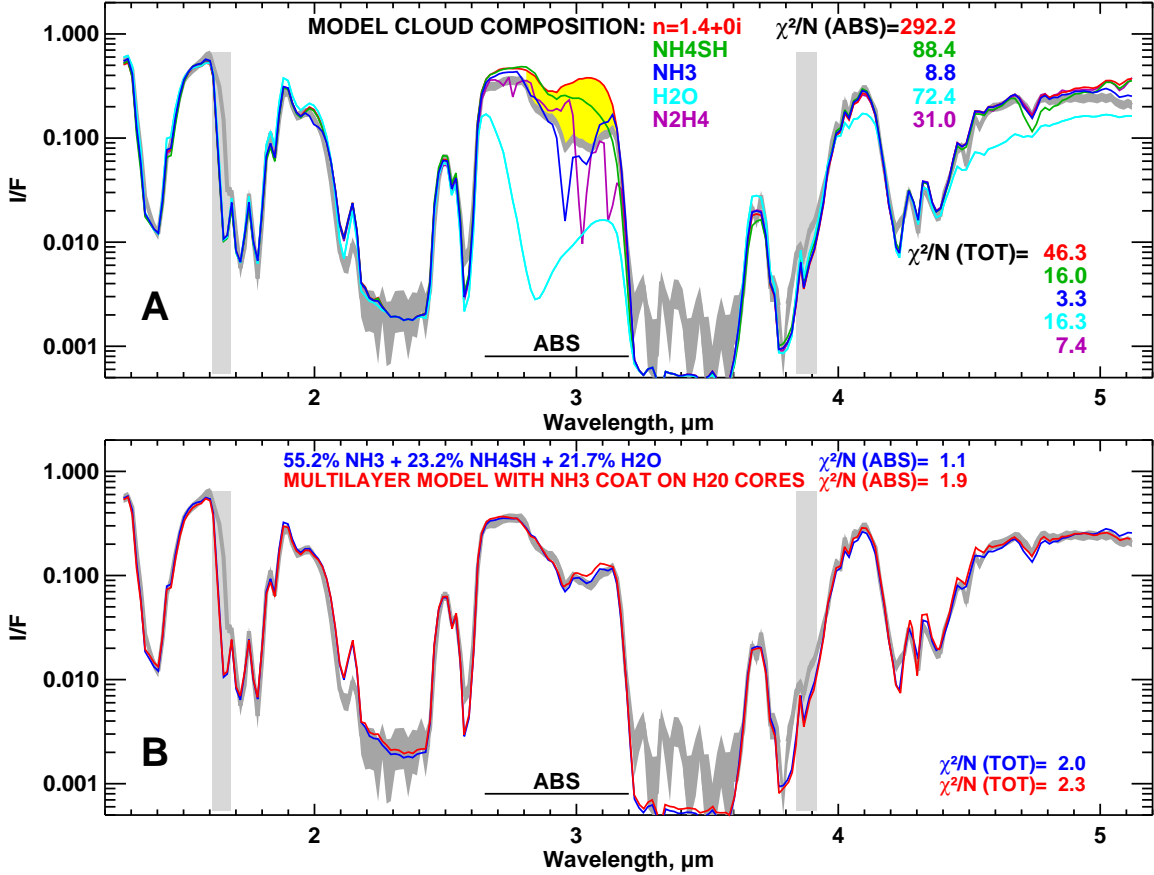


FIG. 12.— (A) A storm head spectrum from (location 1 in Fig. 2), and fits to that spectrum using a main cloud layer consisting of either conservative particles (red), pure  $\text{NH}_4\text{SH}$  particles (green), pure  $\text{NH}_3$  particles (blue), or pure  $\text{H}_2\text{O}$  particles (cyan). The vertical gray bars indicate regions excluded from our analysis because order sorting filter joints lead to uncertain responsivity corrections at those wavelengths. Relative fit quality for each entire pure spectrum (excluding the two regions indicated by vertical gray bars) is indicated by the  $\chi^2/N$  (TOT) values, and for the  $2.65\text{ }\mu\text{m} - 3.2\text{ }\mu\text{m}$  region of particulate absorption by  $\chi^2/N$  (ABS) values, where there are 33 points in the ABS region and 223 in total. The specific fit parameters for each spectrum are given in Table 2. The yellow region between the conservative particle spectrum (red) and the VIMS measured spectrum is due to cloud particle absorption. (B) As in A except that the blue model spectrum is a linear combination of pure spectra, with fractions adjusted to minimize  $\chi^2$  in the particle absorbing (ABS) region, and the red spectrum is for Model 3 (discussed in Section 6.4.3), which is a multi-layer horizontally homogeneous model with the main upper tropospheric haze layer containing an upper sub layer of conservative particles and a lower sub layer of ammonia-coated water ice particles, as defined in Table 6.

than that obtained with conservative particles, mainly due to the better fit in the  $3\text{-}\mu\text{m}$  region, but the fit quality in the  $2.65\text{-}3.2\text{ }\mu\text{m}$  region ( $\chi^2/N$  (ABS) = 88.4) is ten times worse than obtained from pure  $\text{NH}_3$ . It does have a potentially useful characteristic, however. Its I/F at the edge of that window ( $\approx 3.15\text{ }\mu\text{m}$ ) is lower than obtained from  $\text{NH}_3$ , so that combining the two might improve the overall fit quality. While hydrazine ( $\text{N}_2\text{H}_4$ ) provides a decent overall spectral fit, its double absorption peaks in the  $3\text{-}3.2\text{ }\mu\text{m}$  region are a poor match to the observed absorption and also provide little help as a minor contributor.

The fit for pure water ice (cyan curve in Fig. 12A) shows that water is a very strong absorber, with a spectral signature completely different from that of the other substances, and especially different from what is needed to match the observed spectrum. However, it does turn out to have useful properties when we consider composite fits. We often find that good fits using  $\text{NH}_3$  and  $\text{NH}_4\text{SH}$  result in the window regions outside of the  $2.65\text{-}3\text{ }\mu\text{m}$  window being relatively too dark. By adding a small amount of the water spectrum, we can brighten these

window regions without brightening the  $3\text{-}\mu\text{m}$  region because of water's strong absorption at those wavelengths. Incidentally, it may appear strange that water ice fits the observed spectrum better than  $\text{NH}_4\text{SH}$  according to  $\chi^2$  values, yet visually appears to be a much worse fit. The visual appearance is misleading because the plots use a logarithmic y axis, while  $\chi^2$  calculations use a linear weighting of differences (squared).

### 6.3. Linear combination spectral fits

We next consider linear combinations of pure spectra to see if mixed particle compositions could provide a better match than pure particles. These combinations can be thought of as spatially heterogeneous mixtures, perhaps as different particles visible in spaces between clouds of other particles. They are also suggestive of what might happen if an optically thin layer of one cloud type would overlie a layer of another cloud type (but not vertically separated by large distances), or if a cloud consisted of composite particles, perhaps with a core of one (or more) materials with a condensed shell of another material. The best linear combination, shown by the blue

TABLE 2  
ADJUSTABLE FIT PARAMETERS FOR DIFFERENT MAIN CLOUD COMPOSITIONS.

Main cloud composition	Main cloud layer parameter values				
	Top P, mb	Bottom P, mb	Particle radius, $\mu\text{m}$	2- $\mu\text{m}$ Optical depth (2- $\mu\text{m}$ )	$\chi^2$
n=1.4+0i	129 $\pm$ 3	647 $\pm$ 40	1.34 $\pm$ 0.07	12.7 $\pm$ 0.7	538
NH <sub>3</sub>	133 $\pm$ 3	849 $\pm$ 90	1.35 $\pm$ 0.06	18.7 $\pm$ 2.1	426
NH <sub>4</sub> SH	136 $\pm$ 3	945 $\pm$ 120	0.61 $\pm$ 0.01	7.5 $\pm$ 0.7	591
H <sub>2</sub> O	182 $\pm$ 5	401 $\pm$ 60	0.83 $\pm$ 0.10	16.4 $\pm$ 3.7	1274
N <sub>2</sub> H <sub>4</sub>	138 $\pm$ 3	826 $\pm$ 84	1.13 $\pm$ 0.04	13.8 $\pm$ 1.5	479

Fixed parameters included the pressure (2 mb), and 2- $\mu\text{m}$  optical depth (0.01) of the stratospheric haze (assumed to be a conservative, isotropic scatterer with  $\lambda^{-3.5}$  wavelength dependence), and the pressure (1.7 bars), optical depth (100), single-scattering albedo (0.9), and asymmetry parameter (0.6) of the deep cloud. Mie scattering was assumed for the main cloud layer, with equal gas and particle scale heights. Uncertainty limits given here are formal errors useful for relative comparisons only, with no correction to account for excess  $\chi^2$  minima.  $\chi^2$  values listed here are for fits to the 48-wavelength sampled spectra.

TABLE 3  
FIT QUALITY FOR SINGLE-PARTICLE SPECTRA AND BEST FIT COMBINATION SPECTRA.

n=1.4+0i	Component fractions			Fit quality ( $\chi^2/N$ )		Notes
	NH <sub>3</sub>	NH <sub>4</sub> SH	H <sub>2</sub> O	1.26-5.16 $\mu\text{m}$	2.65-3.1 $\mu\text{m}$	
1				46.3	292.2	1
	1			3.3	8.8	1
		1		16.0	88.4	1
			1	16.3	72.4	1
	0.55 $\pm$ 0.04	0.23 $\pm$ 0.02	0.22 $\pm$ 0.02	2.0	1.1	2
0.13 $\pm$ 0.02	0.62 $\pm$ 0.03		0.35 $\pm$ 0.03	2.4	2.9	2
0.00 $\pm$ 0.00	0.83 $\pm$ 0.02	0.17 $\pm$ 0.02		3.7	5.2	2

<sup>1</sup>Fits for single particle types in the main cloud layer, with parameters given in Table 2.

<sup>2</sup>These are linear combination fits with blank columns indicating particle types that were not included in the fit. Here  $\chi^2$  values were computed using the simplified error model described in the text. Note the significant degradation in fit quality when water ice is excluded.

curve in Fig. 12B, uses a mix of 55 $\pm$ 4% NH<sub>3</sub>, 22 $\pm$ 2% water ice and 23 $\pm$ 2% NH<sub>4</sub>SH, where percentages represent fractional area coverage. This improves the fit in the absorbing region to  $\chi^2/N(ABS) = 1.1$ , a factor of 8 better than provided by pure NH<sub>3</sub> (see Fig. 12 caption). A big improvement is also obtained using the conservative (n=1.4) material in place of NH<sub>4</sub>SH, with a mix of 62 $\pm$ 3% NH<sub>3</sub>, 35 $\pm$ 3% water ice, and 13 $\pm$ 2% n=1.4, although the improvement is only by a factor of five in this case. (Uncertainties quoted here are deviations that produce  $\Delta\chi^2 = \chi^2_{MIN}/N$ , where  $N$  is the number of degrees of freedom.) The best linear combination without water ice produced  $\chi^2/N(ABS) = 5.2$ , which is a factor of 5 worse than produced by the best combination with water ice. The water ice component reduces the excess I/F gradient between 3  $\mu\text{m}$  and 3.15  $\mu\text{m}$  and the excess I/F otherwise present between 2.65  $\mu\text{m}$  and 2.85  $\mu\text{m}$ . The third component (either n=1.4 or NH<sub>4</sub>SH) serves to partially fill in the deep minimum produced by pure NH<sub>3</sub> at 2.96  $\mu\text{m}$ . The linear combination analysis clearly favors NH<sub>3</sub>, water ice, and NH<sub>4</sub>SH in that order. Our next step was to determine whether what we think is a somewhat more realistic physical configuration, i.e. a horizontally homogeneous cloud structure, could achieve similar fit quality. The red curve in Fig. 12B is for the last of three such structures we tried.

#### 6.4. Models with composite particles

Numerical experiments with thick layers of coated particles containing substantial fractions of NH<sub>3</sub> as the main tropospheric haze layer produced excessively strong NH<sub>3</sub> signatures unless the fraction of NH<sub>3</sub> was so small that the desirable weaker features were also eliminated. We found a more successful strategy was to split the main tropospheric haze layer into two parts, one basically conservative, and one dominated by NH<sub>3</sub>. There are two relatively plausible implementations of this approach that are both capable of suppressing the stronger NH<sub>3</sub> features while retaining enough of the NH<sub>3</sub> character to match the VIMS observations. The first (Model 1) is to put an optically thin layer of NH<sub>3</sub> particles above a layer with relatively flat spectral properties in the 3- $\mu\text{m}$  region. The second (Model 2) is to put an optically thin layer of conservative particles above an optically thick layer of particles containing a significant component of NH<sub>3</sub>. In the following we consider both options and third (Model 3) that is a variant of the second. The model spectra are compared to the measured storm spectrum in Figs. 13-15, with model vertical structures displayed in Fig. 16. The complexity of these models, involving different materials, different radii, different core fractions and combinations of core and shell materials, as well as optical depth and pressure of each layer, is so large that we cannot demon-

strate uniqueness for any of these solutions.

#### 6.4.1. Model 1: an $\text{NH}_3$ layer on top.

The first model we considered consists of a deep water cloud at 1.2 bars, a main haze sublayer (haze2 in Fig. 13 legend) of composite particles extending between 210 mb and 350 mb, an  $\text{NH}_3$  haze layer from 110 mb to 210 mb, and a stratospheric haze that is of little physical significance because of uncertain I/F measurements at low I/F values. The parameters of this model are defined in Table 4. In Fig. 13 the corresponding model spectrum is compared to the spectrum from the head of the storm. In Fig. 13A we see that the model spectrum does a good job of capturing the main features of the measured spectrum, including the spectral features between 2.9 and 3.1  $\mu\text{m}$ , which are due primarily to  $\text{NH}_3$  ice. No other plausible material in Saturn's atmosphere can produce the sharp feature near 2.96  $\mu\text{m}$  or the secondary bump at 2.05  $\mu\text{m}$ . The  $\text{NH}_3$  layer has a relatively small optical depth ( $\tau=1$ ) so that the underlying bright layer can limit the depth of the sharp absorption feature at 2.96  $\mu\text{m}$ . These  $\text{NH}_3$  ice particles are assumed to be spheres of radius 1.5  $\mu\text{m}$ . We found that significantly larger particles tended to produce too large an I/F at longer wavelengths, while smaller particles made it more difficult to match spectral features near 3  $\mu\text{m}$ .

The underlying layer that provides most of the reflected light visible outside the atmosphere is here composed of composite particles. After trying fits with spectrally flat particles in this layer, we were unable to keep the I/F at 3.1  $\mu\text{m}$  low enough without causing problems at other wavelengths. An example is shown in Fig. 13B, which shows the effects of several different modifications to the nominal compositional model. In one case we used a homogeneous particle of refractive index  $n=1.4$  (computed as a composite particle in which both core and shell are the same), which produces the spectrum shown by the dot-dash curve. This is seen to be too bright at 2.9-3.15  $\mu\text{m}$ , while the fit over the rest of the spectrum is very good. The nominal model, which uses a small core of  $\text{H}_2\text{O}$  (40 $\pm$ 5% of the total radius), takes care of this problem nicely. We also tried to use  $\text{NH}_4\text{SH}$  as a shell material (the dashed curve in Fig. 13B), but this causes problems at many places in the spectrum. Although with some minor adjustment it could produce a reasonable fit in the 2.9-3.1  $\mu\text{m}$  region, it tends to be too bright at 1.9-2.0  $\mu\text{m}$ , at 2.85  $\mu\text{m}$ , and beyond 3.9  $\mu\text{m}$ , as well as being too dark near 3.7  $\mu\text{m}$  because of an absorption by  $\text{NH}_4\text{SH}$  in this region. Some of these problems can be fixed by adjusting other parameters, but we could not find a fix for all of them simultaneously. It is much easier to fit the spectrum using a shell composed of the  $n=1.4$  material that seems to be the main component of clouds in other (non-storm) regions of Saturn's atmosphere.

We also considered a different composition for the deep and optically thick cloud that is mainly needed to block thermal radiation beyond 4.8  $\mu\text{m}$ . Using the  $n=1.4$  material for that cloud produces too high an I/F in the 2.7-2.8  $\mu\text{m}$  region as well as allowing too much thermal radiation to leak through near 5  $\mu\text{m}$ . To fix the thermal leak would require either greatly increased optical depth or an additional absorption. Water fixes both these problems because it has absorption in both regions of the spectrum, while still providing the needed high reflectivity

for the shorter wavelength windows at 1.26  $\mu\text{m}$  and 1.62  $\mu\text{m}$ .

#### 6.4.2. Model 2: conservative particles on top.

Perhaps a somewhat more realistic physical model is the alternate structure summarized in Table 5, with the corresponding spectrum displayed in Fig. 14. In this case the top part of the main cloud layer consists of a pure conservative substance, which we assume to be the same material seen outside of storm regions and is assumed to have a refractive index of  $n=1.4+0i$ . The  $\text{NH}_3$  appears in the lower part of the main cloud layer as a coating on a small core of  $\text{H}_2\text{O}$  (also about 40% of the total radius). The deep layer is composed of pure  $\text{H}_2\text{O}$  ice, as in the previous composite model. This produces a spectral match which is comparable to the first model, but is more easily understood physically. If the storm convection begins at the water cloud level, then as the water particles rise and freeze they will eventually serve as (large) condensation nuclei for  $\text{NH}_3$  which will eventually reach saturation and form a coating on the water cores. This makes more sense than forming coatings of  $n=1.4+0i$  material, since that material is not even known to be formed by condensation at the relevant level of the atmosphere. The top layer of  $n=1.4+0i$  material can perhaps be understood as part of the original main cloud layer pushed to higher altitudes by the convecting tower that brings up water from the deep levels of the atmosphere. This layer has the important spectral effect of filling in the deep minimum at 2.96  $\mu\text{m}$  that would otherwise be visible due to the layer below it, as can be seen from the spectrum in Fig. 14A that is obtained when the layer is removed. Although we do not seem to need  $\text{NH}_4\text{SH}$  or find it useful either in the form of a pure particle or as a coating or core in a two-component composite particle, it is expected that particles are likely to contain a water core, a layer of  $\text{NH}_4\text{SH}$ , followed by a layer of  $\text{NH}_3$ . Unfortunately, we do not have tools for modeling such particles.

#### 6.4.3. Model 3: conservative top layer with an extended deep cloud.

It is also possible and probably more physically realistic to model the deep cloud as vertically extended instead of as a compact layer. Such a model, with a uniform optical depth per bar from the 10 bar level to the bottom of the main (haze2) cloud, can indeed fit the observations just as well as the prior compact model for the deep cloud, as long as the cloud density is sufficient to block out thermal radiation, which requires about 10-20 optical depths per bar. We also found that larger particles in the  $\text{NH}_3$ -containing layer provided a somewhat better match to the spectral features near 3  $\mu\text{m}$ , although maintaining a good overall fit to the spectrum in this case required adding some absorption at long wavelengths. To accomplish that, we made the previously conservative substance absorbing between 4.3 and 5.3  $\mu\text{m}$  by linearly increasing its imaginary index from zero to 0.03 over that region. We also decreased the particle radius in the upper sublayer from 1.5  $\mu\text{m}$  to 1.0  $\mu\text{m}$  to further reduce its reflectivity at longer wavelengths. The model parameters are provided in Table 6. Some of these were fixed manually, while others with uncertainty estimates were adjusted to minimize  $\chi^2$  within the assumed constraints. This revised model is compared with observations in Fig.

TABLE 4  
FIT PARAMETERS FOR COMPOSITE STORM CLOUD STRUCTURE MODEL 1.

Particle Composition	Layer boundaries Ptop Pbottom	Particle radius	Optical depth
NH <sub>3</sub>	110 mb 210 mb	1.50 $\mu\text{m}$	1.0
n=1.4+0i shell on H <sub>2</sub> O core	210 mb 350 mb	1.5 $\mu\text{m}$ with 0.6 $\mu\text{m}$ core	8.0
H <sub>2</sub> O	1000 mb 1200 mb	2.0 $\mu\text{m}$	80

We also included a stratospheric haze between 0.5 mb and 2 mb, which here was treated as a double-HG scatterer with  $\tau=0.01$  at  $2 \mu\text{m}$ , and a  $\lambda^{-3.5}$  wavelength dependence. Nominal gas mixing ratios and profiles were assumed as described elsewhere, except that the PH<sub>3</sub> scale height was assumed to be 50% of the gas scale height.

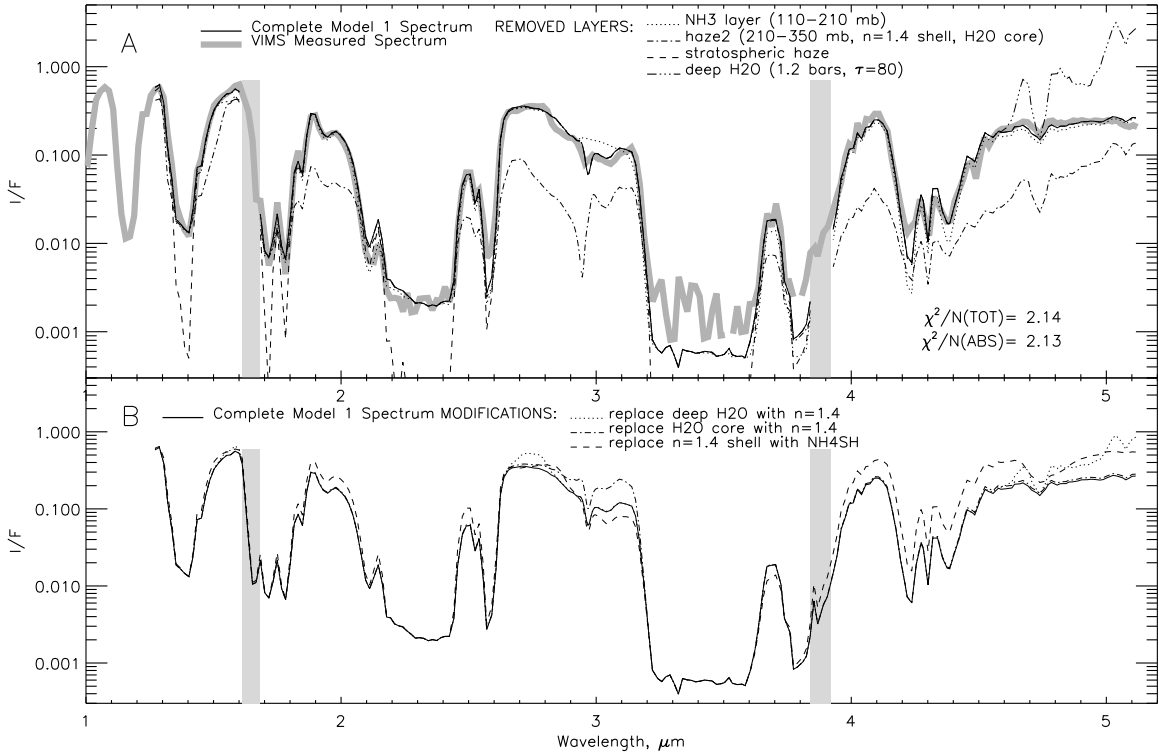


FIG. 13.— A: VIMS measured spectrum of the storm head (thick gray line) in comparison with a complete model spectrum (solid line), and model spectra with different layers removed one at a time (see text for discussion). B: Model spectrum (solid curve) compared to spectra for modified models in which the deep water cloud is replaced by a cloud with  $n=1.4$  (dotted), or the H<sub>2</sub>O core of the 210-350 mb haze is replaced by an  $n=1.4$  core (dot-dashed), or the  $n=1.4$  shell of the 210-350 mb haze particles is replaced by an NH<sub>4</sub>SH shell (dashed). See text for discussion.

15 and also with the best linear combination heterogeneous model in Fig. 12 (red curve). While this provides better fit to the spectrum near  $3 \mu\text{m}$  than the other horizontally homogeneous models, it still does not quite match the quality of the best heterogeneous model. This probably means that there is more physics needed in the homogeneous model to capture more complexity in composition and vertical structure.

Sanz-Requena et al. (2012) analyzed ground-based visual imaging observations covering UV and a range of methane bands for the purpose of characterizing the storm's cloud structure. Their observations were modeled with a 3-layer structure consisting of a stratospheric haze, a tropospheric haze, and a bottom cloud. They

found that the tropospheric haze optical depth was lower in the storm cloud than it was in the non-storm region ( $15 \pm 5$  vs  $25 \pm 5$ ), although the opacity was concentrated at higher altitudes as they inferred a cloud boundary change to 100 - 300 mb (storm) from 100 to  $>1000$  mb (no storm). This concentration of optical depth at low pressures is at least roughly consistent with our inferences from near-IR observations, and also with our finding of a more extended main layer in the non-storm regions. However, as shown in Fig. 16, we find that the storm region is better fit with a two-component main layer, with most of the optical depth in the lower sub-layer, and with the upper sub layer extending to somewhat lower pressures than found in the non-storm regions.



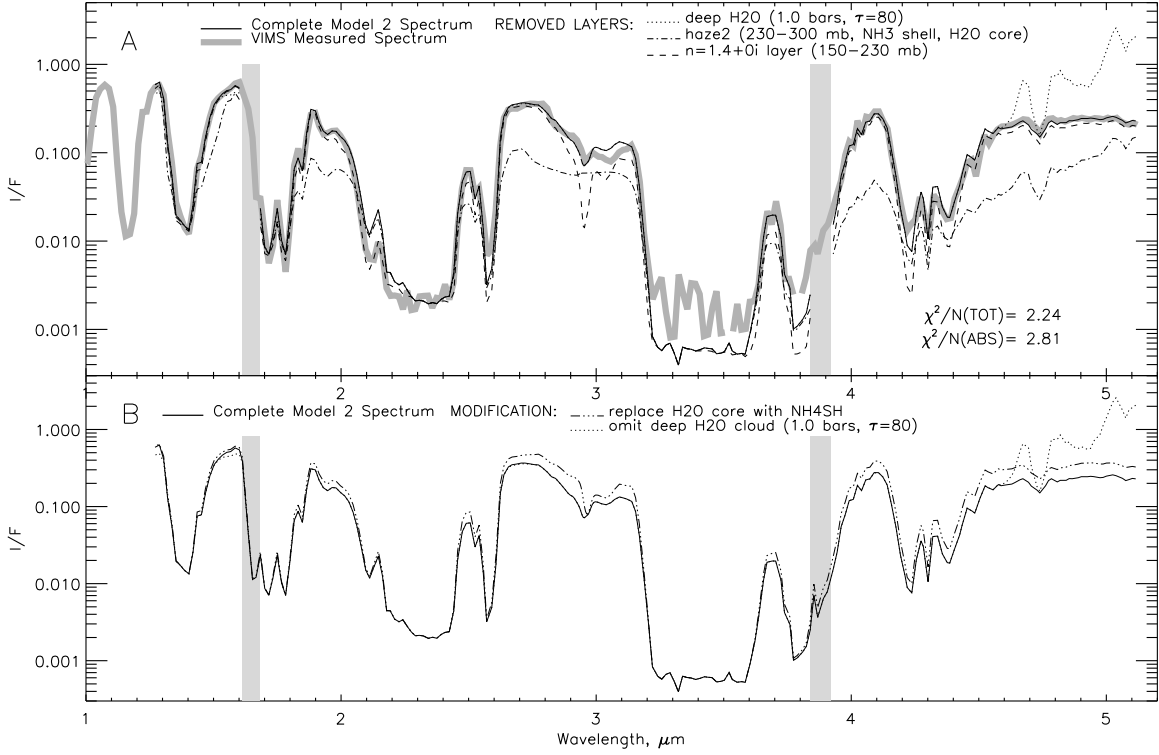


FIG. 14.— A: VIMS measured spectrum of the storm head (thick gray line) in comparison with a complete model spectrum (solid line) for the alternate composite model defined in Table 5; model spectra with different layers removed one at a time are also shown (see text for discussion). The removal of the stratospheric haze layer (not shown) has essentially the same effect as shown in Fig. 13. B: Alternate model spectrum (solid curve) compared to spectra for modifications in which the deep water cloud is removed (dotted), or the H<sub>2</sub>O core of the 230-300 mb haze is replaced by an NH<sub>4</sub>SH core (triple dot-dashed). See text for discussion.

TABLE 5  
FIT PARAMETERS FOR STORM CLOUD COMPOSITE STRUCTURE  
MODEL 2.

Particle Composition	Layer boundaries P <sub>top</sub> P <sub>bottom</sub>	Particle radius	Optical depth
n=1.4+0i	150 mb 230 mb	1.50 $\mu\text{m}$	1.1
NH <sub>3</sub> shell on H <sub>2</sub> O core	230 mb 300 mb	1.5 $\mu\text{m}$ with 0.6 $\mu\text{m}$ core	9.0
H <sub>2</sub> O	900 mb 1000 mb	2.0 $\mu\text{m}$	80

Stratospheric haze and PH<sub>3</sub> scale height as in Table 4

TABLE 6  
FIT PARAMETERS FOR STORM HEAD MODEL 3, WHICH INCLUDES A  
VERTICALLY EXTENDED WATER CLOUD.

Particle Composition	Layer boundaries P <sub>top</sub> , mb P <sub>bot</sub> , mb	Particle radius	Optical depth
n=1.4+0i	140±79 189±25	1.0 $\mu\text{m}$	1.46±0.06
NH <sub>3</sub> shell on H <sub>2</sub> O (core)	189±25 544±135	2.25 $\mu\text{m}$ (0.84 $\mu\text{m}$ )	7.1±1.3
H <sub>2</sub> O	544±135 10 bars	2.0 $\mu\text{m}$	20/bar

Stratospheric haze and PH<sub>3</sub> scale height as in Table 4

## 7. SUMMARY AND CONCLUSIONS

From an analysis of VIMS spectra of the giant Saturn storm of 2010-2011 and its surroundings, we have reached the following conclusions.

1. VIMS spectra outside the storm region exhibit a high degree of uniformity in the fractional depth of a 2.95-3.0  $\mu\text{m}$  absorption feature across the Saturn disk, with essentially no dependence on latitude or view angle, implying that the feature is primarily due to a responsivity error in the vicinity of a 2.98- $\mu\text{m}$  joint between order-sorting filters. It also has a slight variation with the x coordinate of the VIMS images, but essentially no variation with the y coordinate. We developed an accurate correction algorithm that removes this feature, allowing us to detect true absorption by NH<sub>3</sub> in the vicinity of storm clouds.
2. Most near-IR spectra of Saturn outside the storm regions can be very well fit with relatively simple models consisting of (1) a deep and often optically thick cloud layer that serves to block thermal radiation in most places, but is thin enough, or deep enough, in some regions to allow 5- $\mu\text{m}$  detection of atmospheric composition and horizontal structure at the several bar level, (2) a middle “main” cloud layer extending from a top pressure of 111-178 mb to a bottom pressure of 577-844 mb, with optical depths of 3.5-8.6 at 2  $\mu\text{m}$ , and composed of particles that are relatively conservative scatterers, with

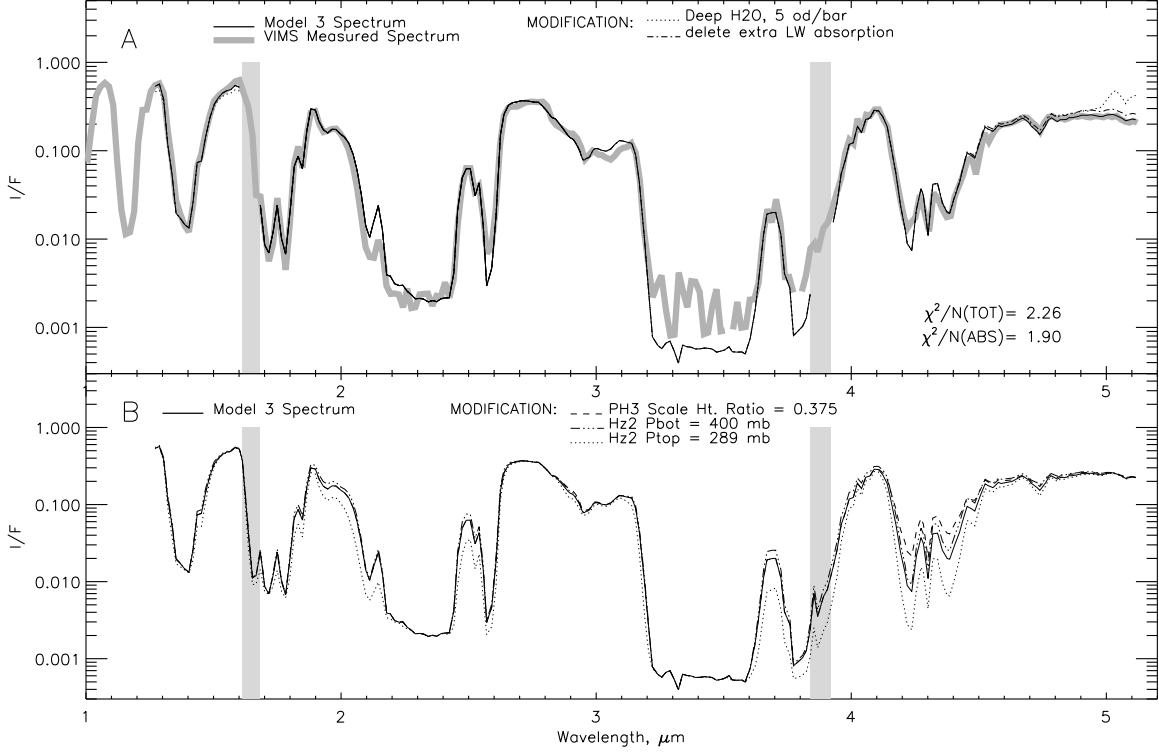


FIG. 15.— A: VIMS measured spectrum of the storm head (thick gray line) in comparison with the model 3 spectrum (solid line), and modified spectra with different values for the optical depth per bar of the vertically extended deep water cloud. B: Model 3 spectrum (solid curve) compared to spectra for modified models with slightly different parameter choices made one at a time. See text for discussion.

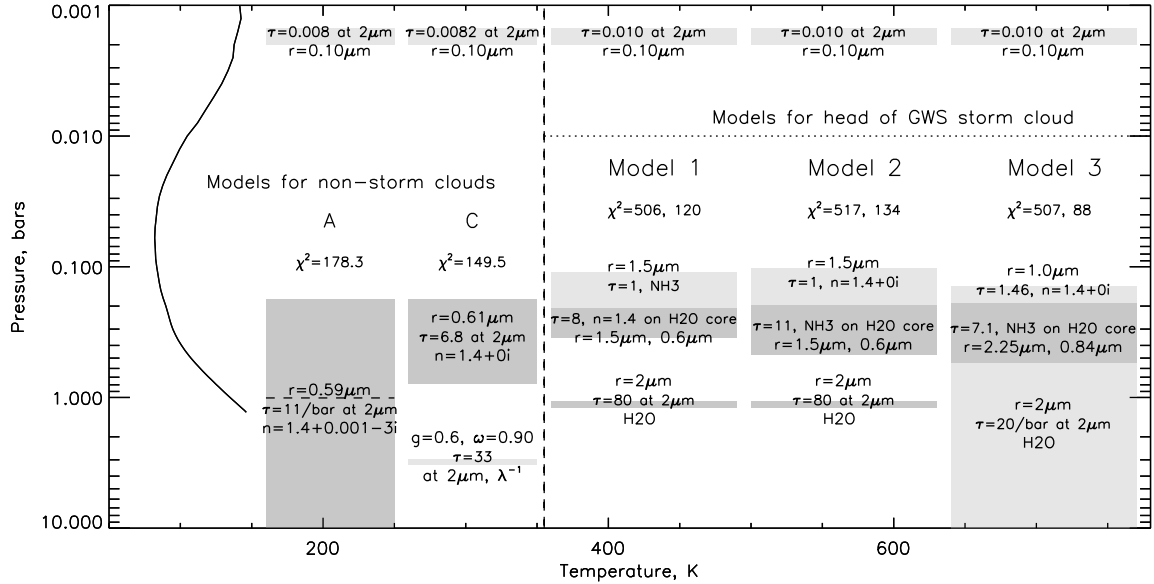


FIG. 16.— Comparison of non-storm cloud structure models A and C (from Fig. 8) with Models 1-3 for the head of the storm. The two  $\chi^2$  values given for Models 1-3 are for the 1.268-5.15  $\mu\text{m}$  region (first) and the 2.65-3.2  $\mu\text{m}$  region (second), with numbers of comparison points being 251 and 51 respectively.

an acceptable refractive index of  $n=1.4+0i$ , and (3) a stratospheric haze of low optical depth, but which cannot be accurately constrained by near-IR VIMS observations because they are too uncertain (and generally too large) at very low I/F values (near the 1 DN level).

3. Outside the storm-affected regions, there is no evidence for particulate absorption at 3  $\mu\text{m}$ , further confirming the peculiar result that at least the upper several optical depths of Saturn's main visible cloud layer is not made of  $\text{NH}_3$ ,  $\text{NH}_4\text{SH}$ , or  $\text{N}_2\text{H}_4$ . We cannot currently rule out  $\text{P}_2\text{H}_4$ , but its pres-

ence seems likely to be testable in the future from measurements near  $4.3\ \mu\text{m}$  once optical constants for solid diphosphine are determined.

4. Inside the storm head we found evidence for a prominent  $3\text{-}\mu\text{m}$  absorber in Saturn's storm clouds but little indication of an absorber active near  $2\ \mu\text{m}$ . A weak  $2\text{-}\mu\text{m}$  feature is not too surprising if the  $\text{NH}_3$  ice is confined to a cloud of relatively small optical depth overlying a relatively bright cloud that fills in the lack of reflectivity in the absorbing regions of the  $\text{NH}_3$  ice spectrum, or if the ammonia-containing cloud layer is underneath a conservative scattering layer that serves the same purpose. An uncovered optically thick layer of pure  $\text{NH}_3$  ice particles would produce a noticeable feature at  $2\ \mu\text{m}$  as well as a very prominent feature  $2.96\ \mu\text{m}$ , and thus a thick cloud of pure  $\text{NH}_3$  ice particles is not plausible as the dominant upper tropospheric cloud in the most absorbing storm regions.
5. We considered four plausible candidate materials that might contribute significant absorption in the  $3\text{-}\mu\text{m}$  region:  $\text{NH}_3$ ,  $\text{N}_2\text{H}_4$ ,  $\text{NH}_4\text{SH}$ , and  $\text{H}_2\text{O}$ . Fits to the observed spectrum outside of the  $2.8\text{--}3.1\ \mu\text{m}$  region of the spectrum were obtained for a model in which each material was taken to be the only component of the main cloud layer. We then compared the features inside  $2.8\text{--}3.1\ \mu\text{m}$  part of the spectrum as well as outside with the VIMS measured spectrum. The only substance that came close to fitting the observed spectrum was  $\text{NH}_3$ , but it had a very sharp absorption feature at  $2.96\ \mu\text{m}$  that was not present in the observed spectrum.
6. We also considered linear combinations of the spectra obtained from the pure composition fits, as might be obtained from a heterogeneous horizontal mix of different particle types. In this case we found that the  $2.96\text{-}\mu\text{m}$  feature could be reduced in amplitude by adding contributions from other materials. The best fits were obtained with a mix of  $\text{NH}_3$ ,  $\text{NH}_4\text{SH}$ , and  $\text{H}_2\text{O}$ , using areal fractions of 0.55, 0.23, and 0.22 respectively.
7. The best fits to VIMS spectra using a horizontally homogeneous vertical structure model contained a deep water cloud, perhaps beginning at 10 bars, but certainly containing significant opacity above the 1-2 bar range, a main cloud layer consisting of two sub-layers, one of low optical depth ( $\tau \approx 1$ ) above a lower sub layer of significant optical depth ( $\tau \approx 9$ ) and an optically thin stratospheric haze that we could not reliably constrain

because of VIMS limitations at very low signal levels. We initially found two options for the main layer produced good fits: (1) particles of  $\text{NH}_3$  ice in the top layer and particles of  $n=1.4$  material (unknown composition also present almost everywhere else on Saturn) coating a core of water ice in the lower sublayer, or (2) particles of  $n=1.4$  in the top sublayer and  $\text{NH}_3$  in the lower sublayer as a coating on  $\text{H}_2\text{O}$  cores, with a core radius that is 40% of the total radius ( $1.5\ \mu\text{m}$ ), and a core volume of 6%. A slightly better fit was obtained with option (2) using smaller particles with some long-wave absorption in the upper main cloud layer and somewhat larger  $\text{NH}_3$ -coated water ice particles in the lower main sub layer.

8. Although  $\text{NH}_4\text{SH}$  was the best third component of our linear combination spectra that represent horizontally heterogeneous mixtures, we did not find a useful role for it in our horizontally homogeneous composite models. It might be present in small amounts in several layers, but when it becomes a significant fraction of the material in the particles, it presents spectral problems that are much easier to solve with other materials. However, it is possible that  $\text{NH}_4\text{SH}$  might prove useful as part of a three-component particle (core with two coatings), which we do not have the tools to model.
9. Both heterogeneous and homogeneous models of the VIMS storm spectra strongly favor contributions by water ice, which is the first strong spectroscopic evidence for water ice in Saturn's atmosphere, found near the level of Saturn's visible cloud deck where it could only be delivered by powerful convection originating from  $\sim 200\ \text{km}$  deeper in the atmosphere, as expected from numerical dynamical models.
10. The increased scale height we found for  $\text{PH}_3$  in the storm head relative to the surrounding regions (0.5 compared to 0.375 times the pressure scale height) is consistent with increased upward convective transport inside the storm.
11. We find strong evidence for the presence of  $\text{NH}_3$  ice at the top of the clouds, but at least some (and perhaps much) of the cloud seems to be of the same relatively conservative (at near-IR wavelengths) material that forms the main component of clouds over the non-storm regions.

#### ACKNOWLEDGMENTS.

Support for this work was provided by NASA through its Outer Planets Research Program under grant NNX11AM58G. We thank two anonymous reviewers for useful suggestions for improving the manuscript.

#### REFERENCES

- Acton, C. H., 1996. Ancillary data services of NASA's Navigation and Ancillary Information Facility. *Planet. and Space Sci.* 44, 65–70.
- Baines, K. H., Delitsky, M. L., Momary, T. W., Brown, R. H., Buratti, B. J., Clark, R. N., Nicholson, P. D., 2009. Storm clouds on Saturn: Lightning-induced chemistry and associated materials consistent with Cassini/VIMS spectra. *Planet. & Space Sci.* 57, 1650–1658.

- Baines, K. H., Momary, T., Fletcher, L., Showman, A., Brown, R., Buratti, B., Clark, R., Nicholson, P., Go, C., Wesley, A., 2011. Saturn's Enigmatic "String of Pearls" and Northern Storm of 2010-2011: Manifestations of a Common Dynamical Mechanism? In: EPSC-DPS Joint Meeting 2011. p. 1658.
- Birnbaum, G., Borysow, A., Orton, G. S., 1996. Collision-Induced Absorption of H<sub>2</sub>-H<sub>2</sub> and H<sub>2</sub>-He in the Rotational and Fundamental Bands for Planetary Applications. *Icarus* 123, 4-22.
- Borysow, A., 1991. Modeling of collision-induced infrared absorption spectra of H<sub>2</sub>-H<sub>2</sub> pairs in the fundamental band at temperatures from 20 to 300 K. *Icarus* 92, 273-279.
- Borysow, A., 1992. New model of collision-induced infrared absorption spectra of H<sub>2</sub>-He pairs in the 2-2.5 micron range at temperatures from 20 to 300 K - an update. *Icarus* 96, 169-175.
- Borysow, A., 1993. Erratum. *Icarus* 106, 614.
- Bowles, N., Calcutt, S., Irwin, P., Temple, J., 2008. Band parameters for self-broadened ammonia gas in the range 0.74 to 5.24  $\mu\text{m}$  to support measurements of the atmosphere of the planet Jupiter. *Icarus* 196, 612-624.
- Briggs, F. H., Sackett, P. D., 1989. Radio observations of Saturn as a probe of its atmosphere and cloud structure. *Icarus* 80, 77-103.
- Brown, R. H., Baines, K. H., Bellucci, G., Bibring, J.-P., Buratti, B. J., Capaccioni, F., Cerroni, P., Clark, R. N., Coradini, A., Cruikshank, D. P., Drossart, P., Formisano, V., Jaumann, R., Langevin, Y., Matson, D. L., McCord, T. B., Mennella, V., Miller, E., Nelson, R. M., Nicholson, P. D., Sicardy, B., Sotin, C., 2004. The Cassini Visual and Infrared Mapping Spectrometer (VIMS) Investigation. *Space Science Reviews* 115, 111-168.
- Butler, R. A. H., Sagui, L., Kleiner, I., Brown, L. R., 2006. The absorption spectrum of phosphine (PH<sub>3</sub>) between 2.8 and 3.7  $\mu\text{m}$ : Line positions, intensities, and assignments. *J. of Molec. Spectrosc.* 238, 178-192.
- Campargue, A., Leshchishina, O., Wang, L., Mondelain, D., Kassi, S., Nikitin, A., 2012. Refinements of the WKMC empirical line lists (5852-7919  $\text{cm}^{-1}$ ) for methane between 80 K and 296 K. *J. Quant. Spectrosc. & Rad. Transf.* 113, 1855-1873.
- Clapp, M. L., Miller, R. E., 1996. Complex Refractive Indices of Crystalline Hydrazine from Aerosol Extinction Spectra. *Icarus* 123, 396-403.
- Colina, L., Bohlin, R. C., Castelli, F., 1996. The 0.12-2.5 micron Absolute Flux Distribution of the Sun for Comparison With Solar Analog Stars. *Astron. J.* 112, 307-315.
- Conrath, B. J., Gautier, D., 2000. Saturn Helium Abundance: A Reanalysis of Voyager Measurements. *Icarus* 144, 124-134.
- Courtin, R., Gautier, D., Marten, A., Bézard, B., Hanel, R., 1984. The composition of Saturn's atmosphere at northern temperate latitudes from Voyager IRIS spectra - NH<sub>3</sub>, PH<sub>3</sub>, C<sub>2</sub>H<sub>2</sub>, C<sub>2</sub>H<sub>6</sub>, CH<sub>3</sub>D, CH<sub>4</sub>, and the Saturnian D/H isotopic ratio. *Astrophys. J.* 287, 899-916.
- Cruikshank, D. P., Meyer, A. W., Brown, R. H., Clark, R. N., Jaumann, R., Stephan, K., Hibbitts, C. A., Sandford, S. A., Mastrapa, R. M. E., Filacchione, G., Ore, C. M. D., Nicholson, P. D., Buratti, B. J., McCord, T. B., Nelson, R. M., Dalton, J. B., Baines, K. H., Matson, D. L., 2010. Carbon dioxide on the satellites of Saturn: Results from the Cassini VIMS investigation and revisions to the VIMS wavelength scale. *Icarus* 206, 561-572.
- Dyudina, U. A., Ingersoll, A. P., Ewald, S. P., Porco, C. C., Fischer, G., Kurth, W. S., West, R. A., 2010. Detection of visible lightning on Saturn. *Geophys. Res. Lett.* 37, L09205.
- Encrenaz, T., Drossart, P., Feuchtgruber, H., Lellouch, E., Bézard, B., Fouchet, T., Atreya, S. K., 1999. The atmospheric composition and structure of Jupiter and Saturn from ISO observations: a preliminary review. *Plan. & Sp. Sci.* 47, 1225-1242.
- Evans, K. F., Stephens, G. L., 1991. A new polarized atmospheric radiative transfer model. *J. Quant. Spectr. and Rad. Trans.* 46, 413-423.
- Fletcher, L. N., Baines, K. H., Momary, T. M., Showman, A. S., Irwin, P. G. J., Orton, G. S., M., R., Merlit, C., 2011a. Saturn's Tropospheric Composition and Clouds from Cassini/VIMS 4.6-5.1  $\mu\text{m}$  Nightside Spectroscopy. *Icarus* 214, 510-533.
- Fletcher, L. N., Hesman, B. E., Irwin, P. G. J., Baines, K. H., Momary, T. W., Sanchez-Lavega, A., Flasar, F. M., Read, P. L., Orton, G. S., Simon-Miller, A., Hueso, R., Bjoraker, G. L., Mamoutkine, A., del Rio-Gaztelurrutia, T., Gomez, J. M., Buratti, B., Clark, R. N., Nicholson, P. D., Sotin, C., 2011b. Thermal Structure and Dynamics of Saturn's Northern Springtime Disturbance. *Science* 332, 1413-1417.
- Fletcher, L. N., Orton, G. S., Teanby, N. A., Irwin, P. G. J., 2009a. Phosphine on Jupiter and Saturn from Cassini/CIRS. *Icarus* 202, 543-564.
- Fletcher, L. N., Orton, G. S., Teanby, N. A., Irwin, P. G. J., Bjoraker, G. L., 2009b. Methane and its isotopologues on Saturn from Cassini/CIRS observations. *Icarus* 199, 351-367.
- Fouchet, T., Moses, J. I., Conrath, B. J., 2009. Saturn: Composition and Chemistry. In: Dougherty, M. K., Esposito, L. W., Krimigis, S. M. (Eds.), *Saturn from Cassini-Huygens*. Springer, Dordrecht, Heidelberg, London, New York, pp. 83-112.
- Frankiss, S. G., 1968. Vibrational Spectrum and Structure of Solid Diphosphine. *Inorg. Chem.* 7, 1931-1933.
- Gautier, D., Conrath, B., Flasar, M., Achterberg, R., Schinder, P., Kliore, A., Cassini Cirs, Radio Science Teams, 2006. The helium to hydrogen ratio in Saturn's atmosphere from Cassini CIRS and radio science measurement. In: 36th COSPAR Scientific Assembly. Vol. 36 of COSPAR Meeting. p. 867.
- Howett, C. J. A., Carlson, R. W., Irwin, P. G. J., Calcutt, S. B., 2007. Optical constants of ammonium hydrosulfide ice and ammonia ice. *Journal of the Optical Society of America B Optical Physics* 24, 126-136.
- Hueso, R., Sánchez-Lavega, A., 2004. A three-dimensional model of moist convection for the giant planets II: Saturn's water and ammonia moist convective storms. *Icarus* 172, 255-271.
- Irwin, P. G. J., Sromovsky, L. A., Strong, E. K., Sihra, K., Bowles, N., Calcutt, S. B., Remedios, J. J., 2006. Improved near-infrared methane band models and k-distribution parameters from 2000 to 9500  $\text{cm}^{-1}$  and implications for interpretation of outer planet spectra. *Icarus* 181, 309-319.
- Karkoschka, E., Tomasko, M., 2005. Saturn's vertical and latitudinal cloud structure 1991-2004 from HST imaging in 30 filters. *Icarus* 179, 195-221.
- Lacis, A. A., Oinas, V., 1991. A description of the correlated-k distribution method for modelling nongray gaseous absorption, thermal emission, and multiple scattering in vertically inhomogeneous atmospheres. *J. Geophys. Res.* 96, 9027-9064.
- Lindal, G. F., Sweetnam, D. N., Eshleman, V. R., 1985. The atmosphere of Saturn - an analysis of the Voyager radio occultation measurements. *Astron. J.* 90, 1136-1146.
- Martonchik, J. V., Orton, G. S., Appleby, J. F., 1984. Optical properties of NH<sub>3</sub> ice from the far infrared to the near ultraviolet. *Appl. Optics* 23, 541-547.
- McCord, T. B., Coradini, A., Hibbitts, C. A., Capaccioni, F., Hansen, G. B., Filacchione, G., Clark, R. N., Cerroni, P., Brown, R. H., Baines, K. H., Bellucci, G., Bibring, J.-P., Buratti, B. J., Bussolletti, E., Combes, M., Cruikshank, D. P., Drossart, P., Formisano, V., Jaumann, R., Langevin, Y., Matson, D. L., Nelson, R. M., Nicholson, P. D., Sicardy, B., Sotin, C., 2004. Cassini VIMS observations of the Galilean satellites including the VIMS calibration procedure. *Icarus* 172, 104-126.
- Miller, E. A., Klein, G., Juergens, D. W., Mehaffey, K., Oseas, J. M., Garcia, R. A., Giandomenico, A., Irigoyen, R. E., Hickok, R., Rosing, D., Sobel, H. R., Bruce, C. F., Flamini, E., Devidi, R., Reininger, F. M., Dami, M., Soufflot, A., Langevin, Y., Huntzinger, G., 1996. The Visual and Infrared Mapping Spectrometer for Cassini. In: Horn, L. (Ed.), *Society of Photo-Optical Instrumentation Engineers (SPIE) Conference Series*. Vol. 2803 of Society of Photo-Optical Instrumentation Engineers (SPIE) Conference Series. pp. 206-220.
- Muñoz, O., Moreno, F., Molina, A., Grodent, D., Gérard, J. C., Dols, V., 2004. Study of the vertical structure of Saturn's atmosphere using HST/WFPC2 images. *Icarus* 169, 413-428.
- Nixon, E. R., 1956. The Infrared Spectrum of Biphosphine. *J. Phys. Chem.* 60, 1054-1059.
- Pérez-Hoyos, S., Sánchez-Lavega, A., French, R. G., Rojas, J. F., 2005. Saturn's cloud structure and temporal evolution from ten years of Hubble Space Telescope images (1994-2003). *Icarus* 176, 155-174.

- Press, W. H., Teukolsky, S. A., Vetterling, W. T., Flannery, B. P., 1992. Numerical recipes in FORTRAN. The art of scientific computing, 2nd ed. Cambridge: University Press.
- Prinn, R. G., Larson, H. P., Caldwell, J. J., Gautier, D., 1984. Composition and chemistry of Saturn's atmosphere. In: Gehrels, T. & Matthews, M. S. (Ed.), Saturn. Univ. of Arizona Press, Tucson, pp. 88–149.
- Rice, J. A., 1995. Mathematical Statistics and Data Analysis, 2nd Edition. Duxbury Press, Belmont, California.
- Rothman, L. S., Gordon, I. E., Barbe, A., Benner, D. C., Bernath, P. F., Birk, M., Boudon, V., Brown, L. R., Campargue, A., Champion, J., Chance, K., Coudert, L. H., Dana, V., Devi, V. M., Fally, S., Flaud, J., Gamache, R. R., Goldman, A., Jacquemart, D., Kleiner, I., Lacome, N., Lafferty, W. J., Mandin, J., Massie, S. T., Mikhailenko, S. N., Miller, C. E., Moazzen-Ahmadi, N., Naumenko, O. V., Nikitin, A. V., Orphal, J., Perevalov, V. I., Perrin, A., Predoi-Cross, A., Rinsland, C. P., Rotger, M., Šimečková, M., Smith, M. A. H., Sung, K., Tashkun, S. A., Tennyson, J., Toth, R. A., Vandaele, A. C., Vander Auwera, J., 2009. The HITRAN 2008 molecular spectroscopic database. *J. Quant. Spectrosc. & Rad. Transf.* 110, 533–572.
- Roux, J. A., Wood, B. E., Smith, A. M., 1979. Optical properties of thin H<sub>2</sub>O, NH<sub>3</sub>, and CO<sub>2</sub> cryofilms. AEDC-TR-79-57. Arnold Engineering Development Center, Tennessee.
- Sánchez-Lavega, A., Colas, F., Lecacheux, J., Laques, P., Parker, D., Miyazaki, I., 1991. The Great White Spot and disturbances in Saturn's equatorial atmosphere during 1990. *Nature* 353, 397–401.
- Sánchez-Lavega, A., del Río-Gaztelurrutia, T., Hueso, R., Gómez-Forrellad, J. M., Sanz-Requena, J. F., Legarreta, J., García-Melendo, E., Colas, F., Lecacheux, J., Fletcher, L. N., Barrado y Navascués, D., Parker, D., International Outer Planet Watch Team, Akutsu, T., Barry, T., Beltran, J., Buda, S., Combs, B., Carvalho, F., Casquinha, P., Delcroix, M., Ghomizadeh, S., Go, C., Hotershall, J., Ikemura, T., Jolly, G., Kazemoto, A., Kumamori, T., Lecompte, M., Maxson, P., Melillo, F. J., Milika, D. P., Morales, E., Peach, D., Phillips, J., Poupeau, J. J., Sussenbach, J., Walker, G., Walker, S., Tranter, T., Wesley, A., Wilson, T., Yunoki, K., 2011. Deep winds beneath Saturn's upper clouds from a seasonal long-lived planetary-scale storm. *Nature* 475, 71–74.
- Sanz-Requena, J. F., Pérez-Hoyos, S., Sánchez-Lavega, A., del Río-Gaztelurrutia, T., Barrado-Navascués, D., Colas, F., Lecacheux, J., Parker, D., 2012. Cloud structure of Saturn's 2010 storm from ground-based visual imaging. *Icarus* 219, 142–149.
- Sill, G., Fink, U., Ferraro, J. R., 1980. Absorption coefficients of solid NH<sub>3</sub> from 50 to 7000 per cm. *Opt. Soc. of Am. J. A* 70, 724–739.
- Sromovsky, L. A., 2005a. Accurate and approximate calculations of Raman scattering in the atmosphere of Neptune. *Icarus* 173, 254–283.
- Sromovsky, L. A., 2005b. Effects of Rayleigh-scattering polarization on reflected intensity: a fast and accurate approximation method for atmospheres with aerosols. *Icarus* 173, 284–294.
- Sromovsky, L. A., Fry, P. M., 2010a. The source of 3- $\mu$ m absorption in Jupiter's clouds: Reanalysis of ISO observations using new NH<sub>3</sub> absorption models. *Icarus* 210, 211–229.
- Sromovsky, L. A., Fry, P. M., 2010b. The source of widespread 3- $\mu$ m absorption in Jupiter's clouds: Constraints from 2000 Cassini VIMS observations. *Icarus* 210, 230–257.
- Sromovsky, L. A., Fry, P. M., Boudon, V., Campargue, A., Nikitin, A., 2012. Comparison of line-by-line and band models of near-IR methane absorption applied to outer planet atmospheres. *Icarus* 218, 1–23.
- Tarrago, G., 1996. Ground State Rotational Energies of Arsine. *J. of Mol. Spectr.* 178, 10–21.
- Toon, O. B., Ackerman, T. P., 1981. Algorithms for the calculation of scattering by stratified spheres. *Appl. Opt.* 20, 3657–3660.
- Warren, S. G., 1984. Optical constants of ice from the ultraviolet to the microwave. *Appl. Optics* 23, 1206–1225.
- West, R. A., Baines, K. H., Karkoschka, E., Sánchez-Lavega, A., 2009. Clouds and Aerosols in Saturn's Atmosphere. In: Dougherty, M. K., Esposito, L. W., Krimigis, S. M. (Eds.), Saturn from Cassini-Huygens. Springer, pp. 161–179.
- Zheng, C., Borysow, A., 1995. Modeling of collision-induced infrared absorption spectra of H<sub>2</sub> pairs in the first overtone band at temperatures from 20 to 500 K. *Icarus* 113, 84–90.